Monthly Notices
of the
ROYAL ASTRONOMICAL SOCIETY

MNRAS **493,** 5273–5289 (2020)
Advance Access publication 2020 February 27

doi:10.1093/mnras/staa469

# The life cycle of the Central Molecular Zone – II. Distribution of atomic and molecular gas tracers

Lucia Armillotta [1,2★] Mark R. Krumholz [1,3] and Enrico M. Di Teodoro [1,4]

[1] *Research School of Astronomy and Astrophysics, The Australian National University, Canberra, ACT 2611, Australia*
[2] *Department of Astrophysical Sciences, Princeton University, Princeton, NJ 08544, USA*
[3] *Centre of Excellence for Astronomy in Three Dimensions (ASTRO-3D), Canberra, ACT 2611, Australia*
[4] *Department of Physics & Astronomy, Johns Hopkins University, Baltimore, MD 21218, USA*

Accepted 2020 February 13. Received 2020 February 4; in original form 2019 November 19

## ABSTRACT

We use the hydrodynamical simulation of our inner Galaxy presented in Armillotta et al. to study the gas distribution and kinematics within the Central Molecular Zone (CMZ). We use a resolution high enough to capture the gas emitting in dense molecular tracers such as $NH_3$ and HCN, and simulate a time window of 50 Myr, long enough to capture phases during which the CMZ experiences both quiescent and intense star formation. We then post-process the simulated CMZ to calculate its spatially dependent chemical and thermal state, producing synthetic emission data cubes and maps of both H I and the molecular gas tracers CO, $NH_3$, and HCN. We show that, as viewed from Earth, gas in the CMZ is distributed mainly in two parallel and elongated features extending from positive longitudes and velocities to negative longitudes and velocities. The molecular gas emission within these two streams is not uniform, and it is mostly associated with the region where gas flowing towards the Galactic Centre through the dust lanes collides with gas orbiting within the ring. Our simulated data cubes reproduce a number of features found in the observed CMZ. However, some discrepancies emerge when we use our results to interpret the position of individual molecular clouds. Finally, we show that, when the CMZ is near a period of intense star formation, the ring is mostly fragmented as a consequence of supernova feedback, and the bulk of the emission comes from star-forming molecular clouds. This correlation between morphology and star formation rate should be detectable in observations of extragalactic CMZs.

**Key words:** hydrodynamics – methods: numerical – stars: formation – Galaxy: centre – Galaxy: evolution.

## 1 INTRODUCTION

The innermost few hundred parsecs region of the Milky Way, the so-called Central Molecular Zone (CMZ, Morris & Serabyn 1996), contains a large reservoir of molecular gas ($M_{\rm CMZ} \sim 2$–$7 \times 10^7\,{\rm M}_\odot$, e.g. Ferrière, Gillard & Jean 2007; Molinari et al. 2011; Longmore et al. 2013a) with properties substantially different from those observed in the Galactic disc. Most of this gas exhibits column and volume densities ∼2 orders of magnitude larger than those measured elsewhere in the disc ($n_{\rm CMZ} \sim 10^4\,{\rm cm}^{-3}$, e.g. Kruijssen & Longmore 2013; Kruijssen et al. 2014; Battersby, Bally & Svoboda 2017), warmer temperatures ($T_{\rm CMZ} \sim 25$–$200$ K, e.g. Ao et al. 2013; Ginsburg et al. 2016; Krieger et al. 2017), and higher level of turbulence (e.g. Shetty et al. 2012; Federrath et al. 2016; Henshaw et al. 2016). Despite the high gas densities, the star formation rate (SFR) in the CMZ is at least one order of magnitude lower than what would be expected if dense gas in the CMZ were to form stars at the same rate as comparably dense gas further out in the disc ($\rm SFR_{CMZ} \sim 0.04$–$0.15\,{\rm M}_\odot\,{\rm yr}^{-1}$, e.g. Yusef-Zadeh et al. 2009; Longmore et al. 2013a; Barnes et al. 2017).

In the last decades, the gas distribution in the CMZ has been extensively studied with the ultimate goal of understanding the characteristics of this extreme environment. Observations of molecular gas tracers, including CO (e.g. Dame, Hartmann & Thaddeus 2001; Oka et al. 2007), $NH_3$ (e.g. Purcell et al. 2012; Krieger et al. 2017), HCN (Jones et al. 2012), and dust tracers (e.g. Rodríguez-Fernández et al. 2004; Molinari et al. 2011) have shown the presence of kinematically coherent structures mostly located within an angular distance of 1° from the Galactic Centre (corresponding to a physical distance of ∼150 pc). Despite the increasing availability of high-resolution data, a detailed characterization of the 3D geometry of the CMZ is still lacking. In fact, our view of the Milky Way through the disc makes extremely difficult to infer the distance of individual gas components from the Sun. Several different interpretations of the gas distribution in the CMZ have been proposed so far, including

★ E-mail: lucia.armillotta@princeton.edu

two spiral arms (e.g. Sofue 1995; Sawada et al. 2004; Ridley et al. 2017), a closed elliptical orbit (Molinari et al. 2011), and an open stream (Kruijssen, Dale & Longmore 2015). Recently, Henshaw et al. (2016) performed a detailed analysis of the molecular gas kinematics in the CMZ, concluding that, among the three mentioned models, the closed elliptical orbit is not able to reproduce the observed data. On the other hand, to distinguish between the other two models, they conclude that proper motion observations are required. The detection of prominent molecular clouds, such as the 20 and 50 km s$^{-1}$ clouds and the dust ridge clouds, in absorption at mid-infrared wavelengths (Molinari et al. 2011) appears to favour the open stream model, which places all these clouds in front of the Galactic Centre. Further constraints on the real position of these clouds with respect to the Galactic Centre are expected to come from measurements of their X-ray emission as a function of time, assuming that this emission is the reflection of X-rays generated by the central massive black hole Sgr A$^*$ during a past outburst (e.g. Clavel et al. 2013; Churazov et al. 2017).

In the absence of direct observational determinations, realistic simulations of Milky-Way-like galaxies can help in interpreting the gas distribution and kinematics within the CMZ. In the first paper of this series (Armillotta et al. 2019, hereafter Paper I), we presented a study of the gas cycle and star formation history within the CMZ through hydrodynamical simulations of the inner region (4.5 kpc from the Galactic Centre) of our Galaxy. In agreement with similar computational works (e.g. Shin et al. 2017; Sormani et al. 2018a; Seo et al. 2019), we found that most of the gas in the CMZ is located in a dense ring-like structure. Such a ring forms in response to the presence of a bar in our Galaxy. In a non-axisymmetric gravitational potential there are two possible families of closed stable orbits: $x_1$ orbits, i.e. orbits elongated parallel to the bar major axis, and $x_2$ orbits, i.e. orbits elongated parallel to the bar minor axis (Binney et al. 1991, see also Kim & Stone 2012; Sormani, Binney & Magorrian 2015; Li et al. 2016). Gas in the outer parts of the bar slowly drifts towards the Galactic Centre following a sequence of $x_1$ orbits. These orbits are more and more elongated as the Galactic Centre is approached. When they become self-intersecting, gas is shocked inwards to $x_2$ orbits and nearly settles into a high-density ring. Depending on local conditions of star formation and stellar feedback, gas may locally depart from $x_2$ orbits, making the overall gas distribution asymmetric. In Paper I, we showed that star formation mostly takes place within the dense ring-like structure, and that is characterized by oscillatory cycles of burst/quenching. Our simulations suggest that the current CMZ is near a minimum of a star formation cycle, in agreement with the findings of earlier analytic and one-dimensional dynamical models by Kruijssen et al. (2014), Krumholz & Kruijssen (2015), and Krumholz, Kruijssen & Crocker (2017).

In this second work, we re-simulate part of the simulation described in Paper I at higher resolution. We then perform detailed observational and chemical post-processing of this new simulation and compare the gas distribution within the CMZ with real observational data. Our goal is three-fold. First, we seek to determine whether our simulation, which reproduces many bulk properties of the observed CMZ quite well, is also able to match the detailed structures found in line maps; in particular, we wish to verify if our hypothesis that the CMZ is currently near a minimum of its star formation cycle is consistent with the available data on gas distribution and kinematics. Secondly, we seek to use the simulations to understand how structures in the position–position–velocity space to which we have observational access map on to structures in physical space. Thirdly, we seek to understand how the observable characteristics of CMZs change over the burst/quench cycle, with the goal of predicting what might be detectable in observations of external galaxies that are at different parts of their cycle than the Milky Way. The paper is organized as follows. In Section 2, we provide a short review of the main observational features of the CMZ to which we will compare our simulation. In Section 3, we describe the main features of the simulation and the details of our chemical and observational post-processing technique. In Section 4, we analyse the synthetic data produced from the simulation. In Section 5, we compare synthetic and observational data and discuss our results in relation to previous works. Finally, in Section 6, we summarize our main findings.

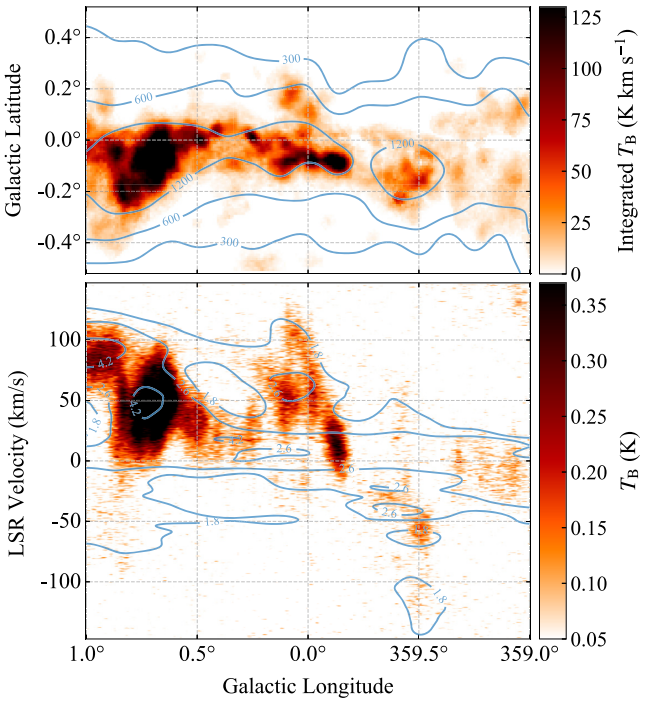


**Figure 1.** Distribution of $NH_3$ (1,1) (heat colour-scale, Walsh et al. 2011; Purcell et al. 2012) and CO ($J = 1 - 0$) (blue contours, Bitran et al. 1997; Dame et al. 2001) emission in the central 2° of the Galaxy. The *upper panel* shows the integrated brightness temperature map over a velocity range ±350 km s$^{-1}$, while the *lower panel* shows the longitude–velocity diagrams averaged over latitude ±0.°5.

## 2 OBSERVATIONAL DATA

In this section, we summarize the main observed features of the CMZ, with the goal of familiarizing readers with the structures to which we will compare our simulations below. We particularly focus on the region at longitude $|l| \leq 2°$ and latitude $|b| \leq 0.5°$ that hosts most of the dense gas emission. Fig. 1 shows the intensity contours of CO ($J = 1 - 0$) emission overlapping the distribution of $NH_3$ (1,1) emission in the region of interest. The CO ($J = 1 - 0$) emission data are taken from the CfA Galactic Plane survey (Bitran et al. 1997; Dame et al. 2001), while the $NH_3$ (1,1) emission data are taken from the $H_2O$ Southern Galactic Plane Survey (HOPS, Walsh et al. 2011; Purcell et al. 2012). The top plot shows the ($l$, $b$) distribution integrated over the local standard of rest (LSR) velocity, $v$, while the bottom plot shows the longitude–velocity distribution, ($l$, $v$), averaged over $b$. The overall emission distribution is similar for the two molecules: it spans ∼200 km s$^{-1}$ in velocity and it is highly

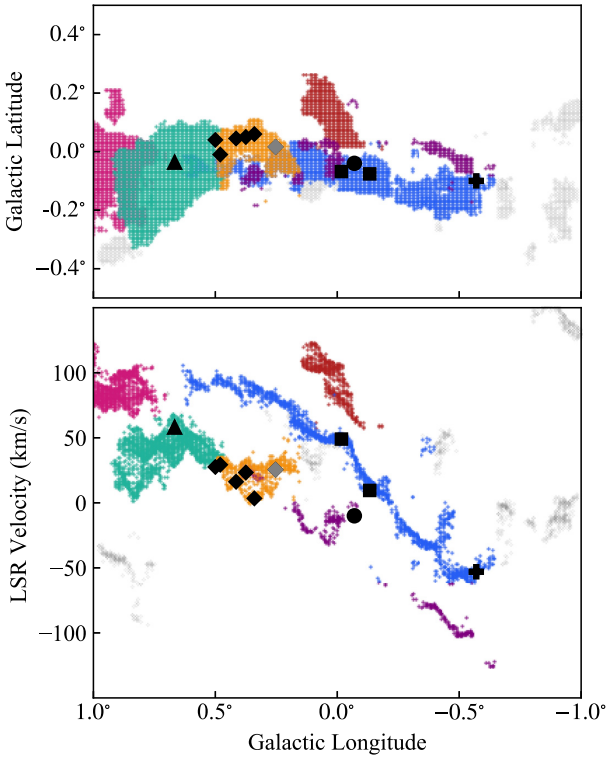


**Figure 2.** ($l$, $b$) (*upper panel*) and ($l$, $v$) (*bottom panel*) distribution of the $NH_3$ (1,1) emission data from the HOPS survey fitted with SCOUSE (Henshaw et al. 2016). The Galactic longitude and latitude of each pixel denote the location of a spectral component with a corresponding best-fitting solution, while the LSR velocity denotes its centroid velocity. The different colours highlight some of the main structures in the ($l$, $b$, $v$) space: Arm I (purple), Arm II (blue), Arm III (red), Sagittarius B2 complex (aqua), dust ridge (yellow), Complex 1.°3 (magenta). The different markers indicate the locations of prominent molecular clouds: Sagittarius B2 (triangle), dust ridge clouds (diamonds), Sagittarius C (cross), 20 and 50 km s$^{-1}$ clouds (squares). The location of Sagittarius A* is denoted with a circle.

asymmetric, with more emission coming from positive longitudes and velocities. We remind readers that $NH_3$ (1,1) traces denser gas than CO ($J = 1 - 0$), and that the former line is usually optically thin, while the latter is certainly optically thick. This explains why the emission peaks of the two molecules do not necessarily coincide.

Fig. 2 shows the $NH_3$ (1,1) data from the HOPS survey fitted with the SCOUSE algorithm (Henshaw et al. 2016). Each point indicates the Galactic longitude, latitude, and centroid line-of-sight velocity of a spectral component as determined by SCOUSE. The different colours highlight some of the main structures in the ($l$, $b$, $v$) data cube, while the different markers represent the location of the most prominent molecular clouds. In the following text, we describe the main properties of these structures (see Henshaw et al. 2016; Longmore et al. 2017, for a detailed description).

(i) *Arm I & II.* Arm I (purple) and Arm II (blue) are two extended and almost parallel features in the longitude–velocity plot ($-0.65° \leq l \leq 0.5°$, $-150\,\mathrm{km\,s^{-1}} \leq v \leq 100\,\mathrm{km\,s^{-1}}$). Sofue (1995) was the first to refer to these structures as 'Arms', since in its interpretation they are two spiral arms within the CMZ.

(ii) *Arm III.* Arm III (red), also known as 'polar arc', is a structure located at high velocities and inclined by >40° with respect to the Galactic plane.

(iii) *Sagittarius B2.* Sgr B2 (aqua colour and black triangle) is a prominent and highly star-forming molecular cloud complex ($0.5° \leq l \leq 0.85°$, $-0.15° \leq b \leq 0.10°$, $10\,\mathrm{km\,s^{-1}} \leq v \leq 70\,\mathrm{km\,s^{-1}}$). It presents a high number of independent velocity components at any given ($l$, $b$) and is characterized by a very broad range of velocity dispersions ($13.3\,\mathrm{km\,s^{-1}} < \sigma < 53.1\,\mathrm{km\,s^{-1}}$, Henshaw et al. 2016). Its complex kinematic structure can explain the shell-like features of Sgr B2, which are thought to be the result of a cloud–cloud collision (e.g. Hasegawa et al. 1994; Sato et al. 2000). A recent alternative interpretation explains the complex structure of Sgr B2 as the superimposition of fragments belonging to the same cloud along the line of sight (Henshaw et al. 2016; Kruijssen et al. 2019).

(iv) *Dust ridge.* Dust ridge (yellow) is the name used to indicate a sequence of molecular clouds (diamonds) located between Sgr2 and G0.253+0.016 (grey diamond), also known as The Brick. The dust ridge clouds appear as absorption features at mid-infrared wavelengths, thus indicating the presence of cold and dense material (Molinari et al. 2011). Kruijssen et al. (2015) and Henshaw et al. (2016) identify two features parallel in velocity in the emission region associated with the dust ridge, suggesting that one of them is probably not associated with the dust ridge clouds.

(v) *20 and 50 km s$^{-1}$ clouds.* The 20 and 50 km s$^{-1}$ clouds (squares) are two bright molecular clouds coherently connected in ($l$, $b$, $v$) space (e.g. Bally et al. 1988; Coil & Ho 2000) located in projected proximity to Sgr A* (circle). A kinematic analysis of their emission shows that they are likely linked to Arm II (Henshaw et al. 2016). Similar to the dust ridge clouds, the 20 and 50 km s$^{-1}$ clouds also appear as absorption features at mid-infrared wavelengths (Molinari et al. 2011).

(vi) *Sagittarius C.* Sgr C (cross) is a molecular cloud complex that is a site of active star formation (e.g. Yusef-Zadeh et al. 2009). The bulk of its emission appears to be kinematically associated with the negative-latitude end of Arm II (Henshaw et al. 2016).

(vii) *Complex 1.3°.* The magenta dots denote the extension at low longitudes of Complex 1.3°, a huge molecular complex that extends over more than 1° in longitude, suggested to be the main accretion site of material on to the CMZ (Rodriguez-Fernandez & Combes 2008).

## 3 METHODS

### 3.1 Numerical scheme

We carry out our simulations using GIZMO (Hopkins 2015), a parallel magnetohydrodynamical code, based on a mesh-free, Lagrangian finite-volume Godunov method. We use the meshless finite mass solver on a reflecting-boundary domain and assume gas to follow an ideal equation of state with a constant adiabatic index $\gamma = 5/3$. We refer the reader to Paper I for a detailed description of the numerical methods used in our simulations. Here, we briefly summarize the relevant features:

(i) *Gravity.* Self-gravity is included in our simulations and it is solved by the Tree method solver described in Springel (2005). In addition to gas self-gravity, our simulations are performed in the presence of an external gravitational potential specific for our problem. We use the best-fitting Milky Way potential by McMillan (2017) as modified by Ridley et al. (2017), which includes contributions from the dark matter halo, the stellar disc, the bulge, and the Galactic bar rotating with a constant patter speed $\Omega_p = 40\,\mathrm{km\,s^{-1}\,kpc^{-1}}$ (e.g. Wegg, Gerhard & Portail 2015).

(ii) *Radiative processes.* Radiative cooling is tracked through the astrophysical chemistry and cooling package GRACKLE (Smith et al. 2017), run in equilibrium mode. GRACKLE provides cooling rates for both primordial species and metals via look-up tables calculated through the CLOUDY spectral synthesis code (Ferland et al. 2013) as a function of temperature and metallicity under the assumption of collisional ionization equilibrium. In addition to radiative cooling, gas can also be heated via diffuse photoelectric heating in which electrons are ejected from dust grains via far-ultraviolet photons. This is implemented as a constant heating rate per hydrogen atom uniformly through-out the simulation box. We use a rate of $8.5 \times 10^{-26}$ erg s$^{-1}$, consistent with the expected heating rate for the inner regions of the Galaxy ($R \sim 3$ kpc, Wolfire et al. 2003).

(iii) *Star formation.* A gas particle can be converted into a star particle if it is: (1) self-gravitating, i.e. virial parameter smaller than 1, (2) dense, i.e. gas density larger than $10^3$ cm$^{-3}$, (3) self-shielded (according to the definition by Krumholz & Gnedin 2011), (4) not photoionized, i.e. gas temperature lower than $10^4$ K. If all these criteria are satisfied, we calculate the probability, $P$, for a given gas particle to be turned into a star as the fraction of gaseous mass that should be converted in stellar mass during the hydro time-step according to the local SFR. The SFR is parametrized as $\dot{\rho}_{\rm SF} = \epsilon_{\rm ff}\rho_{\rm g}/t_{\rm ff}$, where $\rho_{\rm g}$ is the local gas density, $t_{\rm ff} = \sqrt{3\pi/32G\rho_{\rm g}}$ is the local free-fall time, and $\epsilon_{\rm ff} = 0.01$ is the star formation efficiency (this value is chosen based on observational evidence, e.g. Krumholz & Tan 2007; Utomo et al. 2018). If $P$ is larger than a randomly generated number $N \in [0, 1)$, the gas particle is converted into a star particle with the same mass and dynamical properties.

(iv) *Stellar evolution.* We model the time evolution of each newly formed star by using the stellar population synthesis code SLUG (da Silva, Fumagalli & Krumholz 2012; Krumholz et al. 2015). Each star particle spawns an individual SLUG simulation that stochastically draws individual stars from a Chabrier initial mass funtion (Chabrier 2005), tracks their mass- and age-dependent ionizing luminosities, and determines if and when they explode as type II supernovae, along with mass, momentum, and energy injection rates for each supernova. In the SLUG calculations, we use the Padova stellar evolution tracks (Bressan et al. 2012), the 'STARBURST99' spectral synthesis method of Leitherer et al. (1999) and Solar metallicity yields from Sukhbold et al. (2016).

(v) *Stellar feedback.* Simulations include stellar feedback from supernova explosion and photoionization, both of them implemented following the prescriptions in Hopkins et al. (2018a, b). Mass, momentum, and energy injected by each supernova are distributed among the neighbouring gas particles in proportion to the solid angle centred on the star and subtended by the effective face between the gas particle itself and the star. We account for the unresolved energy-conserving phase of the blastwave by imposing a lower limit of $4 \times 10^5$ M$_\odot$ km s$^{-1}$ for the amount of momentum deposited in the ambient medium (see e.g. Kim & Ostriker 2015; Gentry et al. 2019). The ionizing luminosity from each star particle is instead distributed to neighbouring gas particles based on their distance from the star. Starting from the closest, each particle gains the amount of luminosity needed to be ionized, i.e. needed to reach a temperature of $10^4$ K, until the ionizing photon budget is exhausted.

### 3.2 Simulation overview

The initial conditions of the simulation presented in Paper I consist of $2 \times 10^6$ gas particles with mass $2 \times 10^3$ M$_\odot$ distributed in a cylindrical slab with radius 4.5 kpc and half-height 1 kpc and sampled in order to reproduce the mass distribution of the Galactic disc given by Binney & Tremaine (2008). The field velocity is initialized so that gas particles are in radial equilibrium on circular orbits in the axisymmetric part of the gravitational potential of the Galaxy. In the first part of the simulation, gas evolves in the presence of pure hydrodynamics, external gravity, and radiative cooling down to $10^4$ K. Once gas reaches a steady-state equilibrium in the non-axisymmetric part of the gravitational potential, self-gravity, star formation, stellar feedback, and full radiative cooling/heating are switched on.

The left-hand panel of Fig. 3 shows an example of the face-on gas density projection in the central 3 kpc region of the Galaxy. In Section 1, we have briefly explained the gas dynamics in the central region of barred galaxies. Dissipative processes cause material in the outer parts of the bar to slowly flow inwards following $x_1$ orbits. When the $x_1$ orbits become self-intersecting, gas is shocked towards the Galactic Centre, where it settles on to a ring-like structure at $R \sim$ 200–300 pc and approximately follows $x_2$ orbits. The transition from the $x_1$ to the $x_2$ orbits happens through the so-called dust lanes, visible in the left-hand panel of Fig. 3 as dense features connecting gas orbiting at $R \sim 3$ kpc to the central ring. The right-hand panel of Fig. 3 shows the SFR evolution across time in the CMZ region. Burst/quenching cycles of star formation on time-scales of $\sim$50 Myr are mainly driven by supernova feedback instabilities. A comparison with the present-day SFR of the CMZ ($\sim$0.04−0.15 M$_\odot$ yr$^{-1}$, grey bar) suggests that it might lie at a minimum of a star formation cycle.

In this work, we re-simulate part of the simulation presented in Paper I at higher mass resolution, 200M$_\odot$, and lower gravitational softening length, 0.1 pc (i.e. a factor of 10 smaller mass and softening length than our previous simulation). We extract the initial conditions from the low-resolution run at $t = 490$ Myr, i.e. when the SFR is $\lesssim$0.1 M$_\odot$ yr$^{-1}$, and it is therefore representative of the present-day Milky-Way's CMZ, and run the simulation for 50 Myr. The temporal window of the high-resolution simulation is highlighted with an orange bar in the right-hand panel of Fig. 3. We choose our start time and run duration because the SFR increases by one order of magnitude in 50 Myr starting at 490 Myr, so that we will be able to characterize the gas distribution in two very different parts of the CMZ life cycle.

### 3.3 Chemical and observational post-processing

We use the high-resolution simulation of the CMZ to investigate the distribution of H I, CO ($J = 1 - 0$), $NH_3$ (1,1), and HCN ($J = 1 - 0$) emission both in ($x$, $y$, $z$) and ($l$, $b$, $v$) space. The H I emission provides a view of the warmer atomic gas distribution within the CMZ, while the distributions of CO ($J = 1 - 0$), $NH_3$ (1,1), and HCN ($J = 1 - 0$) emission map molecular gas regions at different densities. Among them, the CO ($J = 1 - 0$) transition produces the brightest emission line. However, its relatively low critical density ($\sim$1000 cm$^{-3}$) and generally high optical depth ($\sim$10–100) makes this transition inadequate to trace the high-density gas regions. $NH_3$ (1,1) and HCN ($J = 1 - 0$) transition lines are more suitable to trace gas at densities $\gg 10^3$ cm$^{-3}$. Of these two, the HCN line is generally brighter due to its higher Einstein $A$ coefficient, but by the same token is more vulnerable to optical depth effects.

Since we do not follow the gas chemical evolution in our simulation, we infer the luminosity associated with a given emission line using the post-processing astrochemistry and radiative transfer code DESPOTIC (Krumholz 2014). DESPOTIC calculates the chemical and thermal state of an optically thick spherical cloud given its

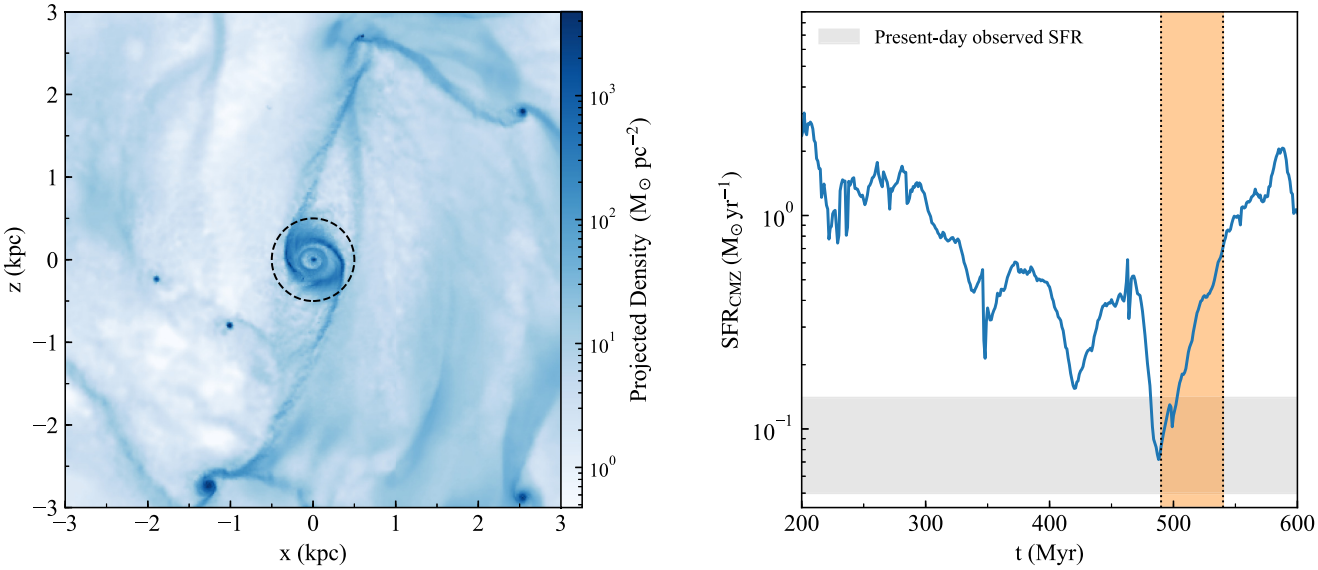


**Figure 3.** Outcomes of the simulation presented in Paper I. *Left-hand panel*: Face-on gas density projection in the central 3 kpc region of the Galaxy. The black dotted circle encloses the region within 500 pc from the Galactic Centre, which we identify as the CMZ. The snapshot have been taken at $t = 500$ Myr. *Right-hand panel*: Time evolution of the SFR in the CMZ. The grey bar indicates the approximate present-day observed SFR. The orange bar encompasses the temporal range between $t = 490$ Myr and $t = 540$ Myr of the high-resolution simulation analysed in this paper.

physical properties (e.g. density, non-thermal velocity dispersion), its chemical composition, the abundances of the elements within it, and the radiation field around it. The chemical equilibrium calculation uses the C-O chemical network of Gong, Ostriker & Wolfire (2017), while the thermal equilibrium calculation includes heating by cosmic rays, grain photoelectric effect, cooling by the lines of H I, C II, C I, O I, and CO, and collisional energy exchange between dust and gas. We use DESPOTIC's large velocity gradient option to calculate optical depths for line cooling, and we adopt Solar abundances for all elements in the chemical network. The nitrogen-bearing species are not included in Gong et al. network, so we assume that these species are present in any gas that is sufficiently shielded for CO to be the main repository of carbon, with the same ratio to CO as is generally found in local observations. Specifically, we adopt $X_{\rm HCN} = X_{\rm NH_3} = 10^{-8}\,(X_{\rm CO}/X_{\rm C})$, where $X_{\rm S}$ indicates the number of members of species S per H nucleus, and $X_{\rm C} = 1.1 \times 10^{-4}$ is the abundance of all carbon atoms regardless of chemical state. Thus, in gas where all carbon is in the form of CO, the abundances of HCN and $NH_3$ are $10^{-8}$; see Offner et al. (2008) and Onus, Krumholz & Federrath (2018) for further discussion of these choices. We refer readers to Krumholz (2014) for details on DESPOTIC in general.

We use DESPOTIC to generate four tables where H I and $H_2$ mass fractions, $X_{\rm H\,I}$ and $X_{\rm H_2}$, CO ($J = 1 - 0$), $NH_3$ (1,1), and HCN ($J = 1 - 0$) transition line luminosities, $L_{\rm CO}$, $L_{\rm NH_3}$ and $L_{\rm HCN}$, and gas temperature, $T_{\rm g}$, are listed as a function of hydrogen number density, $n_{\rm H}$, hydrogen column density, $N_{\rm H}$, and velocity gradient, d$v$/d$r$. Each table is produced assuming a different set of values for the strength of the interstellar radiation field (ISRF), $\chi$, and the primary cosmic ray ionization rate, $\zeta$. We investigate four cases: *Solar* radiation field, $\chi = 1\,G_0$[1] and $\zeta = 10^{-16}$ s$^{-1}$; *weak* CMZ radiation field, $\chi = 10^2\,G_0$ and $\zeta = 10^{-15}$ s$^{-1}$; *intermediate* CMZ radiation field, $\chi = 10^{2.5}\,G_0$ and $\zeta = 10^{-14.5}$ s$^{-1}$; *strong* CMZ radiation field, $\chi = 10^3\,G_0$ and $\zeta = 10^{-14}$ s$^{-1}$. The *Solar* case is representative of the Solar neighbourhood (e.g. van der Tak & van Dishoeck 2000; Le Petit, Roueff & Herbst 2004; Indriolo & McCall 2012). However, the ISRF and the cosmic ray fluxes in the inner regions of the Galaxy are expected to be significantly higher than those measured in molecular clouds in the local disc (e.g. Wolfire et al. 2003); thus, the *Solar* case is provided solely as a baseline for comparison. Unfortunately, ionization rates and ISRF strengths in the CMZ region are poorly constrained, and are in reality probably not uniform in space or time. Published estimates span at least a factor of 10, depending on the technique used and the region being observed. Our range from *weak* to *strong* cases is intended to be roughly representative of the range of published estimates (e.g. Clark et al. 2013; Ginsburg et al. 2016; Oka et al. 2019). We discuss the choice of radiation field model further in Appendix A, where we show that our *intermediate* case provides the best overall fit to the present-day CMZ, and that it successfully reproduces bulk properties such as the total molecular gas mass and CO luminosity. We therefore adopt this choice for all the results presented in the main text, deferring discussion of how the results depend on the radiation field to the appendix.

We post-process the simulation outcomes to calculate $X_{\rm HI}$, $X_{\rm H_2}$, $T_{\rm g}$, $L_{\rm CO}$, $L_{\rm NH_3}$, and $L_{\rm HCN}$ as follows. We first compute the values of $n_{\rm H}$, $N_{\rm H}$, and d$v$/d$r$ for each gas particle and then perform a trilinear interpolation on the DESPOTIC tabulated values. The hydrogen number density is calculated as

$$n_{\rm H} = \frac{\rho \mu_{\rm H}}{m_{\rm H}}, \tag{1}$$

where $\rho$ is the local gas density associated with the gas particle, $\mu_{\rm H} = 0.71$ is the hydrogen mass fraction assuming Solar metallicity and $m_{\rm H} = 1.67 \times 10^{-24}$ g is the mass of the hydrogen nucleus. The hydrogen column density is defined as in Safranek-Shrader et al. (2017),

$$N_{\rm H} = n_{\rm H} L_{\rm shield}, \tag{2}$$

where $L_{\rm shield}$ is the shielding length. Post-processing of galactic-disc-scale simulations with ray-tracing-based radiative transfer and

[1] $G_0$ corresponds to the ISRF strength given in Draine (1978).

chemical network integration have shown that local models with photoshielding based on equation (2) reproduces the distribution and amount of molecular gas reasonably well as compared with a detailed, global ray-tracing calculation. Specifically, an approach based on the Jeans length ($L_{\rm shield} = L_{\rm J} = \pi c_{\rm s}^2/G\rho$, where $c_{\rm s}$ is the local adiabatic sound speed) with a $T = 40$ K temperature cap yields the most accurate $H_2$ and CO abundances (Safranek-Shrader et al. 2017). Finally, the velocity gradient is calculated as

$$\frac{{\rm d}v}{{\rm d}r} = \|\nabla \otimes \boldsymbol{v}\| \equiv \sqrt{\sum_{i,j=1}^{3} \left(\frac{\partial v_i}{\partial x_j}\right)^2}, \tag{3}$$

where $\boldsymbol{v}$ the local gas velocity associated with the gas particle.

Once the chemical post-process of the simulation is computed, we calculate the ($l$, $b$, $v$) gas particle distributions for each simulation snapshot. We assume that the Sun is undergoing circular motion in the Galactic plane at a radius $R_\odot = 8$ kpc with speed $v_\odot = 240\,{\rm km\,s^{-1}}$ and that the angle between the bar major axis and the Sun-Galactic Centre line is 20° (e.g. Bland-Hawthorn & Gerhard 2016). We bin the gas particles within 500 pc from the Galactic Centre in ($l$, $b$, $v$) space. The resolution of each bin is $\Delta l = 0.015°$, $\Delta b = 0.015°$, and $\Delta v = 1\,{\rm km\,s^{-1}}$. In each bin, we sum the brightness temperatures associated with the CO ($J = 1 - 0$), $NH_3$ (1,1), and HCN ($J = 1 - 0$) emissions, $T_{\rm B,\,CO}$, $T_{\rm B,NH_3}$ and $T_{\rm B,\,HCN}$, respectively, and the H I column density, $N_{\rm HI}$, over all the gas particles within the bin. The brightness temperature is calculated as

$$T_{\rm B}[{\rm K}] = \frac{\lambda^2}{2k_{\rm B}} \frac{L}{4\pi D^2 \Delta\nu} \frac{180^2}{\pi^2 \Delta l \Delta b}, \tag{4}$$

where $\lambda$ is the wavelength associated with the line transition, which is 0.26 cm for the CO ($J = 1 - 0$) transition, 1.27 cm for the $NH_3$ (1,1) transition, and 0.34 cm for the HCN ($J = 1 - 0$) transition), $k_{\rm B} = 1.38 \times 10^{-16}\,{\rm erg\,K^{-1}}$ is the Boltzman constant, $L$ is the emission-line luminosity in ${\rm erg\,s^{-1}}$ associated with each gas particle, $D$ is the distance of the gas particle from the Sun in cm, and $\Delta\nu = 10^5 \Delta v/\lambda$ is the frequency resolution. The H I column density of each particle is calculated as

$$N_{\rm H\,I} = n_{\rm H\,I}\, h = X_{\rm H\,I} n_{\rm H}\, h, \tag{5}$$

where $h \equiv (M/\rho)^{-1/3}$ is the spatial resolution scale (average inter-particle separation around the gas particle), with $M$ the gas particle mass. We calculate the H I column density, rather than the luminosity associated with the H I-21 cm transition, since this is more informative. However, converting the H I column density into luminosity is straightforward since H I is mostly optically thin (Dickey & Lockman 1990).

## 4 SIMULATION ANALYSIS

Before analysing the post-processed gas distribution, we give an overview of the CMZ evolution throughout the high-resolution simulation. Note that in the simulation we identify the central 500 pc region as CMZ. The left-hand panel of Fig. 4 shows the SFR versus time (blue line). The simulation experiences a brief burst of star formation as soon as we increase the mass resolution / decrease the softening length. However, after a few Myr stellar feedback pushes the system back towards equilibrium, and the SFR drops to values comparable to those found at matching times in the lower resolution simulation. From that point on, the SFR increases as a function of time, going from $\sim$0.1–0.2 $M_\odot\,{\rm yr^{-1}}$ to 1–2 $M_\odot\,{\rm yr^{-1}}$ in 20–30 Myr. For comparison, we show the SFR as a function of time in the low-resolution simulation (dotted orange line). The time-averaged trends are very similar at the two different resolutions, but in the high-resolution case the SFR fluctuates more rapidly since we can capture deeper collapses followed by more effective episodes of feedback from the resulting highly clustered stars. We refer readers to Appendix A of Paper I for a more thorough discussion on the resolution-dependence of our results.

In the right-hand panels of Fig. 4, we show the CMZ gas density distribution in two different moments of the star formation activity. When the level of star formation is low (SFR $\sim$0.2 $M_\odot\,{\rm yr^{-1}}$ at $t = 505$ Myr), most of the gas lies in a highly dense ($\Sigma_{\rm gas} \gtrsim 10^3\,M_\odot\,{\rm pc^{-2}}$) elliptical ring located at $\sim$200–300 pc from the Galactic Centre. In addition to the main ring, we can note the presence of a less dense ring/spiral-like structure located at $\sim$100 pc from the Galactic Centre. We identify this gas with the wake of a massive molecular cloud ($M \geq 10^7\,M_\odot$) tidally destroyed by its encounter with the Galactic Centre (see Section 3.2 in Paper I) in the low-resolution run. The gas configuration is completely different when the CMZ is actively star-forming (SFR $\sim$2 $M_\odot\,{\rm yr^{-1}}$ at $t = 530$ Myr). Supernova feedback associated with the intense star formation activity enhances the level of turbulence, thus disrupting the dense ring. The new gas configuration consists of a number of molecular clouds rotating nearly in the same position of the former ring and surrounded by more diffuse turbulent gas.

In the following text, we focus on the analysis of the post-processed simulation in the two different moments of the CMZ life, close to the minimum (Section 4.1) and the maximum (Section 4.2) of the star formation activity, and on the dense gas evolution across time (Section 4.3).

### 4.1 Low SFR: synthetic maps

In Fig. 5, we present a view of the CMZ at $t = 505$ Myr as seen through different gas tracers. The top panels show the Cartesian distribution of H I number density and CO ($J = 1 - 0$), $NH_3$ (1,1), and HCN ($J = 1 - 0$) luminosity taken at $z = 0$. The central and bottom panels show the distribution of $N_{\rm HI}$, $T_{\rm CO}$, $T_{\rm NH_3}$, and $T_{\rm HCN}$ in the ($l$, $v$) and ($l$, $b$) diagram, respectively. We decide to not plot the gas distribution in the central few pc of the Galaxy. This region is unresolved in our simulations and, since we do not include the gravitational potential of the black hole that dominates the central few pc, the dynamics within it is not reliable. The distributions in the ($l$, $v$) diagram have been averaged over $b = \pm 0.5°$, while the distributions in the ($l$, $b$) diagram have been integrated over $v = \pm 200\,{\rm km\,s^{-1}}$. The maps are not colour-coded in regions where the gas temperature calculated by DESPOTIC is above $2 \times 10^4$ K, i.e. when gas is fully ionized. DESPOTIC is indeed not intended to work at such temperatures. We observe that the dense structures in the ($l$, $v$) diagram show low velocity dispersion compared to the observed data (see Fig. 1). Indeed, due to the finite simulation resolution, we cannot trace the velocity distribution on scales smaller than the spatial resolution scale, thus the line-of-sight velocity component associated with each gas particle shows a delta-function profile rather than a Gaussian-like profile.

The first thing to note from Fig. 5 is that the molecular ring formed in our simulation extends from $l = 2.5°$ to $l = -2.5°$. In Sections 1 and 2, we have seen that most of the molecular gas in the CMZ is observed within an angular distance of 1° from the Galactic Centre. Thus, the size of the dense ring in our simulation is more than a factor of 2 larger. This is because the gravitational potential used in our simulation was built to be consistent with large-scale properties of the Milky Way, but it was not fine-tuned to

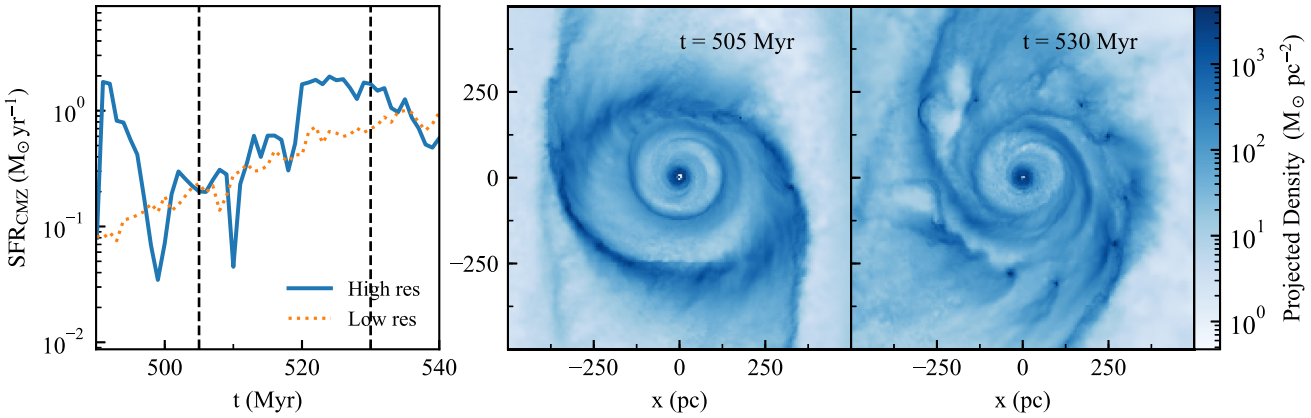


**Figure 4.** CMZ region in the high-resolution simulation discussed in this paper. Time evolution of the SFR (blue solid line, *left-hand panel*) and face-on gas density projection at two different times, $t = 505$ Myr (*middle panel*) and $t = 530$ Myr (*right-hand panel*). The orange line shows the time evolution of the SFR in the low-resolution simulation (see Fig. 3). The two dashed lines in the SFR plot indicate the SFR values at the times when the two snapshots have been taken.

reproduce the observed extension of the CMZ. Recently Sormani et al. (2019) have modified the bar parameters in Ridley et al. gravitational potential to match the observed size of the CMZ. They have performed simulations similar to ours, but without self-gravity and stellar feedback, and found that the CMZ gas configuration produced in response to the new gravitational potential is a smaller ring structure in better agreement with the observed CMZ size. However, the small inconsistency between our adopted global potential and the observed ring size should have relatively small effects on the dense gas, whose properties are more sensitive to self-gravity and feedback than to the overall potential.

In the top panels of Fig. 5, we can observe how the emission produced by each gas tracer is distributed within the CMZ ring. Among the molecular gas tracers, the CO ($J = 1 - 0$) transition produces the brightest emission throughout the entire ring. However, given its low critical density, this transition is inadequate to map the high-density gas regions. For example, the bright filament in the upper side of the ring appears smooth and uniform in the $L_{CO}$ map, while its clumpy internal structure is well resolved in the $L_{NH_3}$ and $L_{HCN}$ maps. The emission associated with $NH_3$ (1,1) and HCN ($J = 1 - 0$) is indeed able to map denser and isolated structures within the ring. The H I distribution traces the diffuse atomic gas. Its density peaks in the gas envelope surrounding molecular clouds.

In the longitude–velocity diagrams, we identify the presence of two nearly parallel elongated features extending from positive longitudes and velocities to negative longitudes and velocities. Their emission is more or less continuous depending on the gas tracer. We use the left-hand panel of Fig. 6 to identify corresponding structures in ($x$, $y$) and ($l$, $v$) space. The top feature (colour-coded in blue) corresponds to the ring side closer to the Sun, while the bottom feature (colour-coded in red) corresponds to the ring side farther from the Sun. Gas rotates clockwise, moving from positive longitudes and velocities to negative longitudes and velocities in the near ring side, and from negative longitudes and velocities to positive longitudes and velocities in the far ring side. Although the velocity field of $x_2$ orbits is symmetric with respect to the bar axes, the two sides of the ring appear as two offset features in the ($l$, $v$) plane because the orbit is elliptical and the Sun-Galactic Centre line is not aligned with one of the two axes of the ellipse. As a consequence, the line of sight crosses the two sides of the orbit at points that are not symmetric with respect to the axes of symmetry of the ellipse,[2] which results in a different projected rotational velocity for gas on the near and far sides.

The H I distribution is nearly uniform, thus allowing us to identify the entire ring structure in the longitude–velocity map. The emission appears less uniform in the CO map and it is predominantly clumpy in the $NH_3$ and HCN diagrams. The non-uniform molecular gas distribution is the consequence of non-uniform star formation, which leads to different local conditions of turbulence, radiative cooling and gravity within the ring. Asymmetries in the CMZ were also found in the simulations with no self-gravity and stellar feedback performed by Sormani et al. (2018a). However, in such simulations asymmetries develop due to the combination of thermal instability and the so-called wiggle instability. We can observe that the emission associated with the bottom stream is brighter compared to the top stream, especially at positive longitudes and velocities, corresponding to the ring region connected to the dust lanes (see Section 4.3 for a more accurate analysis of these bright high-density structures). Finally, the low-density inner ring at $R \sim 100$ pc (colour-coded in yellow in Fig. 6) appears as a less inclined feature in the H I ($l$, $v$) map, but its emission becomes weaker and weaker moving towards dense gas tracers. We point out that the match in extension between the inner ring formed in the simulation ($|l| \leq 1°$) and the observed CMZ is just a coincidence and no connection can be traced between these two structures. The observed CMZ is indeed highly dense and star-forming, similarly to the external ring formed in the simulation.

In the longitude–latitude diagrams, we observe that the ring is slightly tilted with respect to the Galactic plane, especially on the positive longitude side. The $NH_3$ and HCN emission peaks, corresponding to the densest structures in the CMZ, are located within $\pm 0.05°$ from the plane.

[2]Note that this statement should in principle be valid even though the Sun-Galactic Centre line was aligned with one of the two bar axes. Since individual lines of sight diverge from the Sun-Galactic Centre line with increasing distance from the Sun, they should intercept non-axisymmetric points on the near and far sides of elliptical orbits. However, the CMZ extension is so small compared to the Sun-Galactic Centre distance that the lines of sight intercepting the CMZ can be considered almost parallel, and thus this effect is small. The majority of the splitting in the ($l$, $v$) plane therefore is due to the offset between the ellipse axis and the sightline, rather than due to the divergence of sightlines.

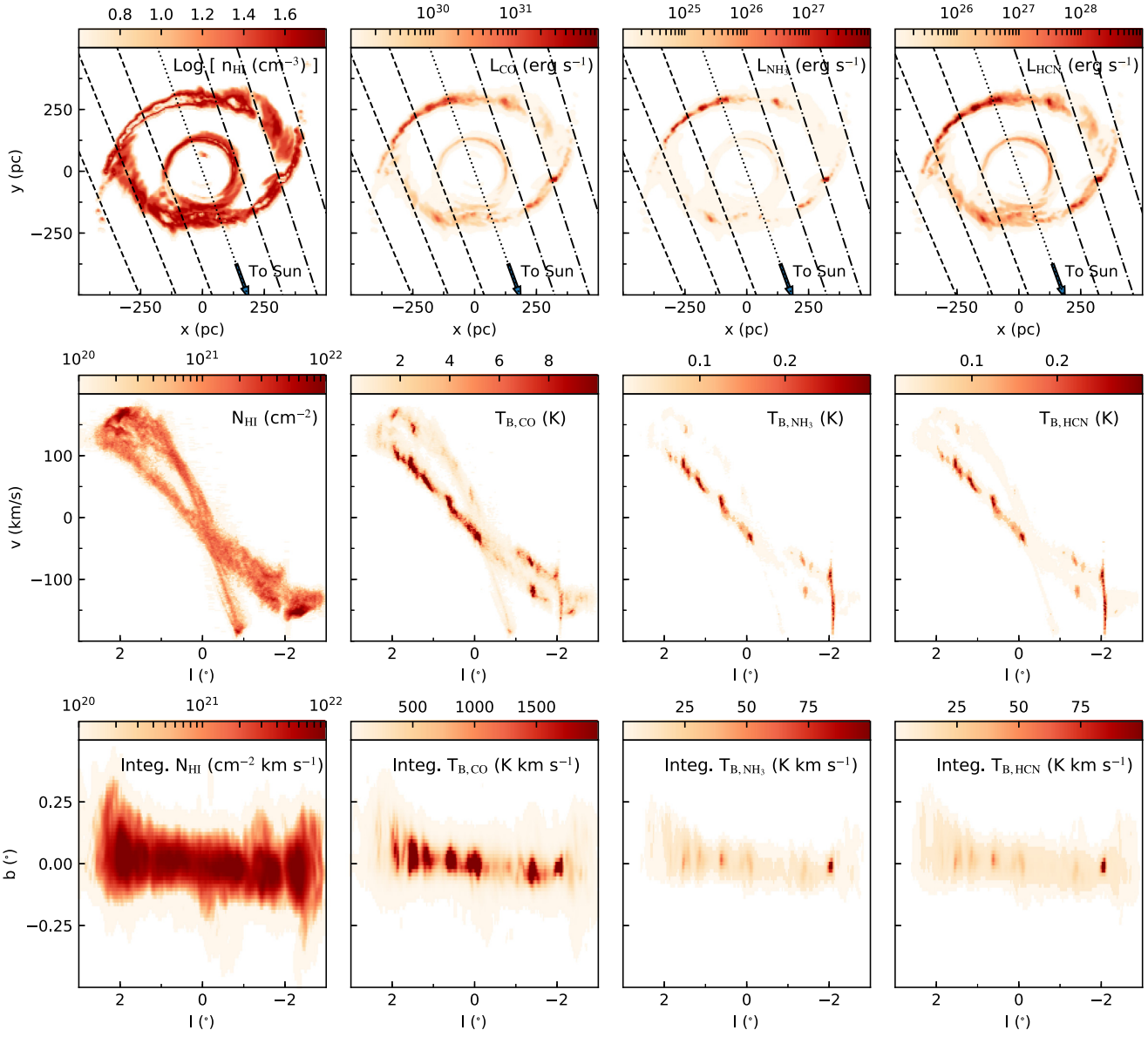


**Figure 5.** *Top panels*: from left to right snapshots taken at $z = 0$ of H I number density, $n_{\rm HI}$, CO ($J = 1 - 0$) luminosity, $L_{\rm CO}$, $NH_3$ (1,1) luminosity, $L_{\rm NH_3}$, and HCN ($J = 1 - 0$) luminosity, $L_{\rm HCN}$. The bar major axis is aligned with the axis $x = 0$. In each plot, the dotted black line indicates the line connecting the Sun to the Galactic Centre, $l = 0$, while the dashed/dot–dashed line indicate the line of sights at $l = \pm 1°, 2°, 3°$. The arrow points towards the Sun position. *Central panels*: from left to right longitude–velocity distributions of H I column density, $N_{\rm H\,I}$, CO ($J = 1 - 0$) brightness temperature, $T_{\rm CO}$, $NH_3$ (1,1) brightness temperature, $T_{\rm NH_3}$, and HCN ($J = 1 - 0$) brightness temperature, $T_{\rm HCN}$, averaged over the latitude range $\pm 0.5°$. *Bottom panels*: from left to right ($l$, $b$) maps of $N_{\rm HI}$, $T_{\rm CO}$, $T_{\rm NH_3}$, and $T_{\rm HCN}$, integrated over the velocity range $\pm 200$ km s$^{-1}$. The gas distribution is analysed at $t = 505$ Myr.

### 4.2 High SFR: synthetic maps

Fig. 7 is the same as Fig. 5, but at $t = 530$ Myr. As anticipated in Fig. 4, the gas distribution is much less uniform when the CMZ is actively star-forming because feedback associated with the star formation activity shreds the dense ring. The lack of a coherent structure is clearly visible also in the more diffuse atomic gas phase. In the H I ($l$, $v$) plot, the two parallel and elongated features present at $t = 505$ Myr are replaced by multiple ridges of gas with lower extension in longitude and velocity, corresponding to fragments of the previous ring, or by arc-like structures (e.g. structure at $v \sim 100$–$150$ km s$^{-1}$ and $l \sim 2°$), corresponding to gas compressed by supernova explosions. The low-density inner ring is the only structure that is much the same in Fig. 5 as in Fig. 7, since no star formation occurs in it.

Strong $NH_3$ and HCN emission is produced by dense and star-forming molecular clouds. In the ($l$, $v$) plot, these clouds appear like features with narrow longitude range and broad velocity dispersion ($\sigma \lesssim 50$ km s$^{-1}$). Although high velocity dispersions are in fact measured in the Milky-Way CMZ (e.g. Sgr B2, see Section 2), we stress that the internal dynamics of the high-density clouds produced in our simulation are unreliable. As already discussed in Paper I, gas at sufficiently high density is not resolved due to the presence of softened gravity, which prevents structures smaller than the gravitational softening length from forming. In the simulation analysed in this paper the softening length is 0.1 pc. In a

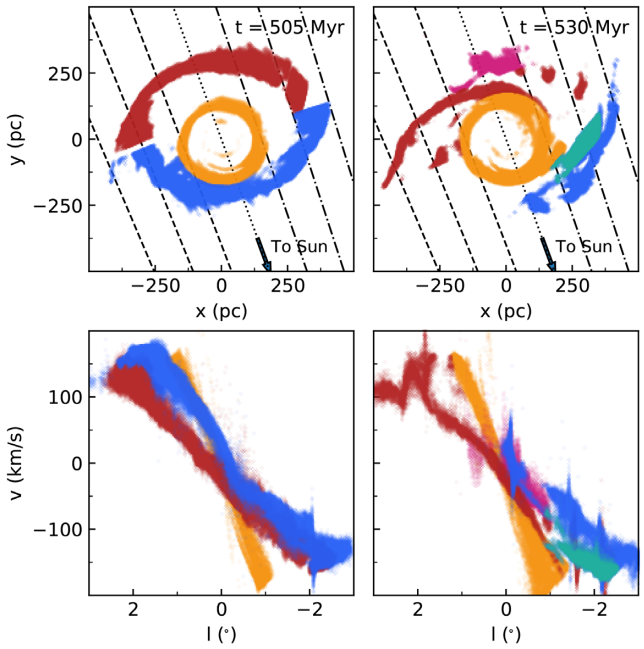


**Figure 6.** Gas particle distribution colour-coded to identify corresponding structures in the $(x, y)$ and $(l, v)$ space at $t = 505$ Myr (*left-hand panels*) and $t = 530$ Myr (*right-hand panels*). Only gas particles identified by DESPOTIC as atomic and molecular gas are shown.

Lagrangian code, like GIZMO, the inter-particle separation is directly related to the gas density, $h \equiv (M/\rho)^{-1/3}$. Thus, given our mass resolution of 200 $M_\odot$, the distance between gas particles approaches the gravitational smoothing length when $n_H \gtrsim 10^6$ cm$^{-3}$. We therefore underestimate the velocity dispersion of gas approaching this density.

Finally, in the right-hand panels of Fig. 6, we note that, despite the much less coherent gas distribution, gas located on the near side with respect to the Sun is still characterized by line-of-sight velocities higher than those of gas located on the far side at equal longitude. This is because the centres of mass of individual gas clumps nearly rotate on elliptical $x_2$ orbits (see also Sormani et al. 2018a, for similar results).

### 4.3 High-density gas evolution

In this section, we focus on the high-density gas ($n_H \gtrsim 10^3$ cm$^{-3}$) evolution and its distribution in longitude–velocity space. Fig. 8 shows the time evolution of the CMZ region seen through different indicators. The first panel of each row shows the velocity field overlapping the hydrogen gas number density distribution in the frame co-rotating with the bar. The second panel shows the virial parameter, $\alpha_{vir}$, distribution for gas at $n_H \geq 10^3$ cm$^{-3}$, which gives an indication of the gravitational stability of the gas. The virial parameter is defined as

$$\alpha_{vir} = \frac{(dv/dr)^2 + (c_s/h)^2}{8\pi G\rho}. \quad (6)$$

The third panel shows the HCN ($J = 1 - 0$) luminosity distribution, while the fourth panel displays the HCN ($J = 1 - 0$) brightness temperature $(l, v)$ map. We investigate the temporal range between 505 and 510 Myr, i.e. when the SFR is roughly consistent with the present-day value.

As anticipated in Section 4.1, the longitude–velocity HCN distribution is highly asymmetric, and most of the emission comes from the ring regions immediately connected to the dust lanes (see Figs 5 and 6). A comparison between the $n_H$ and $L_{HCN}$ maps shows that this region is actually very dense ($n_H \gg 10^3$ cm$^{-3}$). In this region, gas flowing towards the Galactic Centre through the dust lanes collides with gas orbiting within the ring, thus enhancing the local gas density. An example is provided in the panels at $t = 508$ Myr and $t = 509$ Myr. We highlight two regions in the $L_{HCN}$ and $T_{B,\,HCN}$ maps at $t = 508$ Myr: the region connected to the dust lane (blue ellipse) in the ring side near the Sun and a dense cloud (blue circle) which is crushing into it. This collision results in an increase of the gas density and emission at $t = 509$ Myr. Fig. 8 shows however that features such as this are not necessarily present at other times. For example, at $t = 505$ Myr the $(l, v)$ plot is characterized by a bright ridge of clouds at positive longitudes associated with the ring side far from the Sun. This feature is however not equally visible at later times.

A second important conclusion that one can draw from Fig. 8 is that the high-density regions formed as a consequence of gas collisions do not always evolve as gravitationally bound structures. We can see this by following the evolution of a gas cloud (indicated with a green circle in the $\alpha_{vir}$, $L_{HCN}$ and $T_{B,\,HCN}$ maps) from $t = 505$ Myr to $t = 507$ Myr. During its trajectory, the cloud emission luminosity becomes weaker and weaker, going from $\sim 10^{28}$ erg s$^{-1}$ at $t = 505$ Myr, to a few times $10^{26}$ erg s$^{-1}$ at $t = 507$ Myr. This decrease in luminosity is the consequence of the cloud evaporating over time. Indeed, although it has a high initial density, $n_H \sim 7 \times 10^3$ cm$^{-3}$ at $t = 505$ Myr, the cloud is borderline gravitationally bound, $\alpha_{vir} \sim 0.5$–1. We remind readers that $\alpha_{vir} = 1$ for a gas cloud in virial equilibrium between turbulent motions and gravity. The cloud density is therefore not high enough to gravitationally confine the cloud against turbulent motions. Densities larger than $10^4$ cm$^{-3}$ are required for the gravitational collapse to start. An example is provided by the cloud highlighted with a black circle at $t = 509$ Myr and $t = 510$ Myr, whose virial parameter is $\sim$0.1–0.2. The high density required to overcome the high level of turbulence explains the low level of star formation the CMZ ring is undergoing in this temporal range of the simulation. Gas at densities of $\gtrsim 10^3$ cm$^{-3}$ elsewhere in the Galaxy is almost all self-gravitating and thus star-forming, but this is not true in the much more turbulent environment of the CMZ.

## 5 DISCUSSION

### 5.1 Comparison with the observations

In this section, we use the results of our post-processed simulation when the SFR is near the minimum to interpret and spatially locate the observed features discussed in Section 2. As noted above, we cannot do a one-to-one comparison because we have not tuned the global potential to exactly reproduce the observed ring size. Moreover, we have seen that much of the dense gas structure is highly time dependent, and so even if we matched the global size, we would not expect to reproduce every feature. Instead, our goal is to identify analogous structures in the simulated and real CMZ, and use these to interpret the observations.

Our synthetic data have shown that the dense CMZ ring produces two extended and almost parallel features in the longitude–velocity diagram. To a different extent, these two features are traced both from atomic gas and molecular gas emission. We identify these two features with Arm I and Arm II observed in the present-day

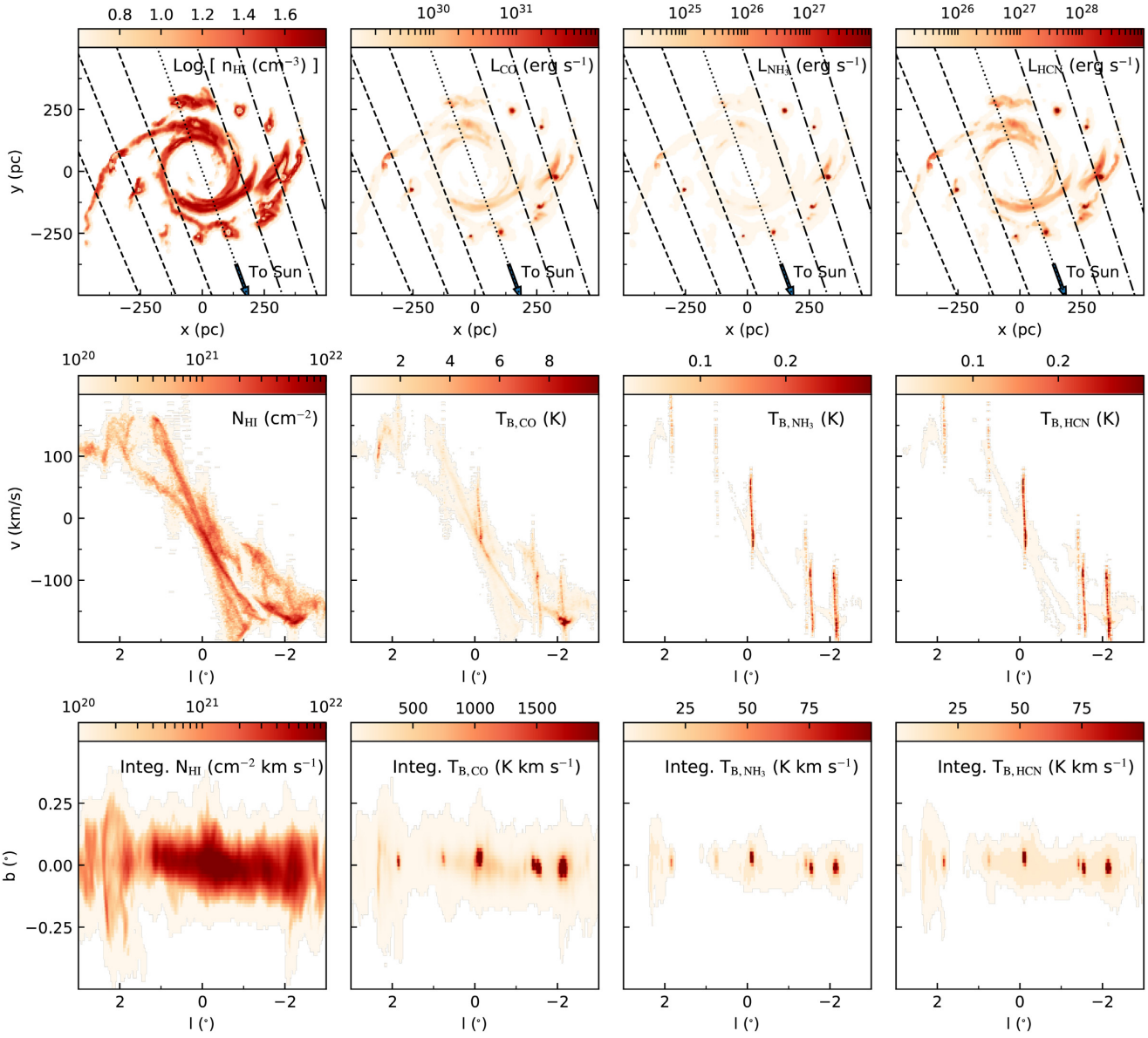


**Figure 7.** Same as Fig. 5, but at $t = 530$ Myr.

CMZ. Arm I would be associated with the ring side far from the Sun, while Arm II would be associated with the ring side near the Sun. This allows us to locate Sgr C and the 20 and 50 km s$^{-1}$ clouds on the near side of the ring, because, as we have seen in Section 2, their emission is kinematically associated with the Arm II emission. This is in agreement with the geometry proposed by Henshaw et al. (2016), who argued that the 20 and 50 km s$^{-1}$ clouds are situated on the near side of the CMZ because they appear to correspond to absorptions features at 70 μm (Molinari et al. 2011).

Given their alignment in longitude and velocity with Arm I, we might deduce that Sgr B2 and the dust ridge molecular clouds are a continuation of Arm I, and therefore located on the far side of the CMZ. In this sense, their location on the high longitude and velocity side of Arm I would be in agreement with what observed in Sections 4.1 and 4.3, i.e. that most of the molecular gas emission associated with the far side of the ring comes from the region at higher longitudes as a consequence of cloud–cloud collision at the dust lane-ring interception. The hypothesis that Sgr B2 is the result of cloud–cloud collisions was already proposed in the past to explain its complex kinematic structure with multiple velocity components (e.g. Hasegawa et al. 1994; Sato et al. 2000). Observational studies have shown that Sgr B2 is undergoing intense star formation activity (e.g. McGrath, Goss & De Pree 2004; De Pree et al. 2014), suggesting that the collision has involved a very dense, perhaps already star-forming, cloud. On the other side, the dust ridge molecular clouds present little or no signs of star formation activity, although they have both high masses and low temperatures (e.g. Lis et al. 2001; Immer et al. 2012). The dust ridge clouds might be identified with the weakly bound molecular clouds discussed in Section 4.3 (see also the cloud highlighted with a green circle in Fig. 8), which are supported against collapse by their high levels of internal turbulence.

There are two main observational constraints that are difficult to reconcile with our picture of Sgr B2 and the dust ridge molecular clouds as being located on the far side of the CMZ. First, the

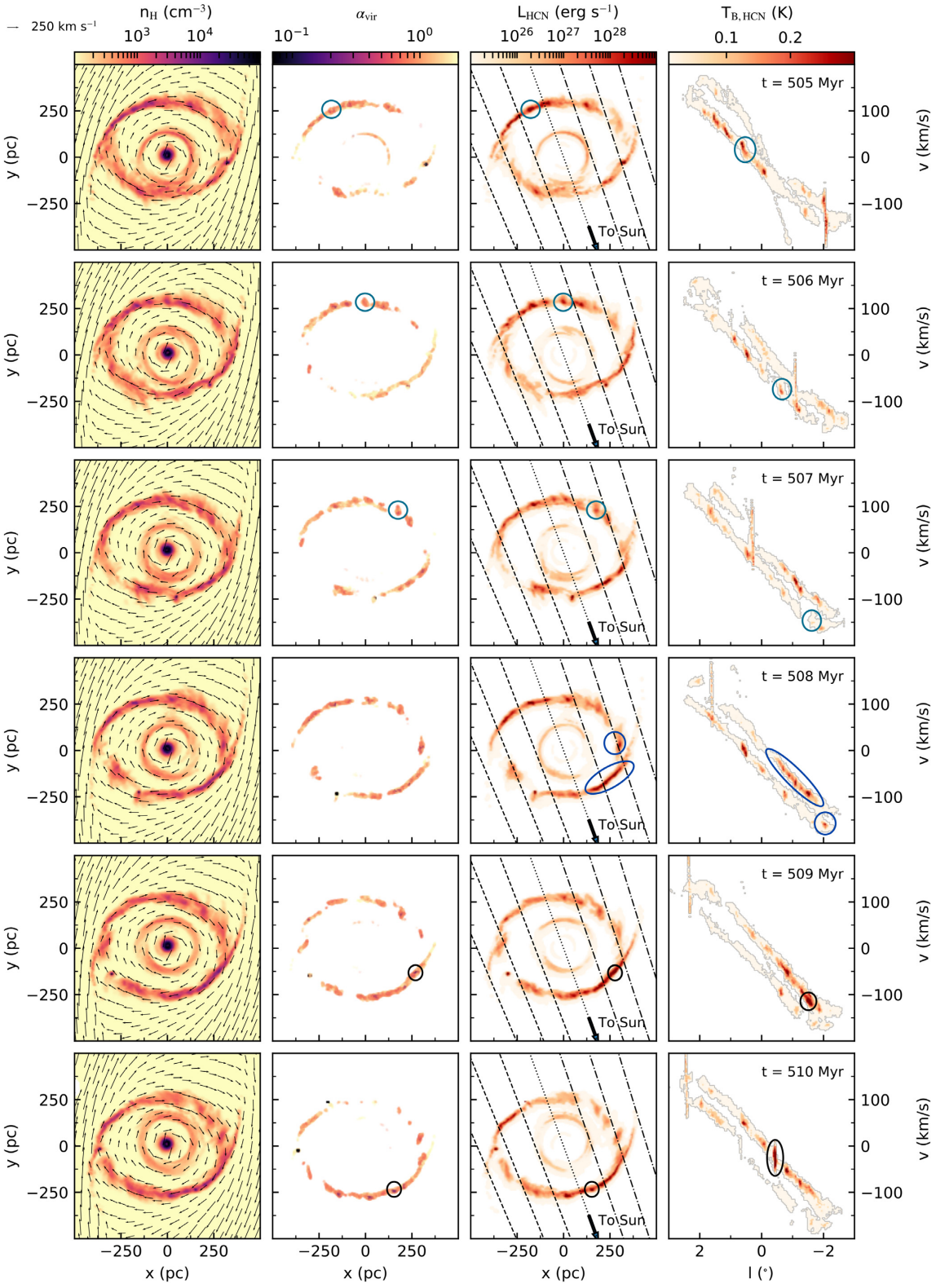


**Figure 8.** Temporal sequence of snapshots taken at $z = 0$. Each row shows the Cartesian distribution of $n_{\rm H}$ (*first column*), virial parameter (*second column*), $L_{\rm HCN}$ (*third column*), and the ($l$, $v$) distribution of $T_{\rm B,\,HCN}$ (*fourth column*) at a given time. The time at which the snapshots have been taken is indicated in the last panel of each row. In the first panel of each row the velocity field overlaps the $n_{\rm H}$ distribution. The velocity field is shown with vectors, whose length indicates the velocity magnitude. The coloured contours denote relevant structures discussed in the main text.

dust ridge clouds appear to correspond to absorption features at 70 μm, much like the 20 and 50 km s$^{-1}$ clouds. This would place the cloud on the near side of the CMZ, based on the assumption that clouds behind the Galactic Centre are obscured from the CMZ IR emission. While this is suggestive, and is certainly a concern for our interpretation, we also caution that we have little information about the 3D dust and IR source distribution in the inner 1° from the Galactic Centre, and thus inferences about near-side versus far-side based on the presence of IR absorption features are necessarily tentative. A second constraint is given by the observed proper motion of two water masers in Sgr B2 that indicate that this region is moving towards higher longitudes (Reid et al. 2009). However, the small number of observed sources implies large uncertainties, especially because water masers are often associated with high-velocity outflows from young stellar objects and, in this case, they might not be representative of the overall motion of Sgr B2. If a proper motion towards positive longitudes were proven true, our interpretation that Sgr B2 is rotating towards lower longitudes in the far side of the ring would certainly be disproved. However, in this case, our interpretation of Arm I and II as the two sides of the ring could still be consistent with the observational constraints if we were to assume that Sgr B2 and the dust ridge clouds are detached from the bulk of the gas rotating on $x_2$ orbits by stellar feedback. Such detached clouds occur regularly in our simulations in the aftermath of periods of high star formation activity, when feedback locally destroys the ring-like gas distribution (see Section 4.2).

We do not identify structures with features similar to those of Arm III and Complex 1.3° in our post-processed CMZ. In the H I and CO longitude–velocity diagrams, we have identified the low-inclination gas stream at negative longitude as the inner low-density ring at $R \sim 100$ pc. This might be compared with Arm III, which presents a similar structure in the ($l$, $v$) plot, even though located at positive velocities. However, there are two main inconsistencies between the feature in our simulation and Arm III. The first one is that we do not observe the inner ring in the $NH_3$ and HCN maps, since its density is not high enough ($n_H \lesssim 10^3$ cm$^{-3}$) to be detected through high-density gas tracers. This inconsistency would be overcome if we post-processed the simulation with a model based on a less intense radiation field, which might be reasonable since no star formation occurs in the inner ring (see Fig. A2 and Appendix A). The main inconsistency with the observation is however that, unlike Arm III, the inner ring in not inclined with respect to the Galactic plane in the ($l$, $b$) diagram. Concerning Complex 1.3°, this has been suggested to be the accretion site of material on the CMZ. In our model, gas accretes on to the CMZ through the dust lanes. As before, the dust lane region approaching the ring is not visible through high-density gas tracers in our post-processed CMZ. However, they could be detected assuming a less intense radiation field, as we show in Appendix A. We cannot further speculate on the possible connection of Complex 1.3° with the dust lanes, since we have restricted our analysis to the ring region only, without post-processing the outer parts of the Galaxy.

Finally, from the analysis of the synthetic ($l$, $b$) maps, we have seen that, similar to what is observed in the present-day CMZ, clumps of dense gas are distributed within a few parsecs above and below the plane, suggesting that their orbits are not perfectly aligned with the Galactic plane. However, the observed CMZ presents a larger extension in latitude compared to the simulation. For example, Sgr B2 extends over $-0.15° \leq b \leq 0.1°$, while in the simulation the densest structures are located at $|b| \leq 0.05°$.

### 5.2 Comparison with previous works

Different models have been proposed to interpret the 3D gas distribution within the CMZ. In agreement with our model, the 'elliptical orbit' model proposed by Molinari et al. (2011) predicts that the CMZ represents an elliptical ring of gas moving on $x_2$ orbits. In this model, all the prominent molecular clouds (see Section 2) are located on the near side of the ring, to be consistent with the assumption that the dust ridge clouds and the 20 and 50 km s$^{-1}$ clouds appear as absorption features at 70 μm because they lie in the front side of the ring. The main difference from our model is that Molinari et al. (2011) assumed a constant orbital velocity, while in our simulation the orbital velocity varies depending on the orbital phase angle. In particular, it increases in proximity of the minor axis, and decreases in proximity of the major axis.

To give an idea of how different configurations of rotational velocity affects the gas distribution in ($l$, $v$) space, in Fig. 9, we show simplified ring models in both ($x$, $y$) and ($l$, $v$) space. In the first column from the left, we model an orbit with variable rotational velocity ($v_{rot} \propto a/R$, where $a$ is the size of the minor semi-axis), representative of our simulation. In the second column, we model an orbit with constant orbital velocity, representative of the Molinari et al. model. In both the examples, the angle between the bar major axis and the Sun-Galactic Centre line is 20°. The model with constant orbital velocity still produces two elongated features in the ($l$, $v$) map, corresponding to the near and far side of the ring. However, their profiles present more asymmetries in velocity compared to the model with variable velocity. We highlight that, given the alignment of the minor axis of the $x_2$ orbit with the bar major axis, the stream at higher line-of-sight velocities always corresponds to the near side of the ring, regardless of the velocity field. The first and second top panels of Fig. 9 clearly show that the projection of the orbital velocity on the line of sight is larger for gas on the near side of the ring. The opposite would be true if the major axis of the elliptical orbit were aligned with the bar major axis (see third and forth column of Fig. 9). This configuration would be however inconsistent with the dynamical studies predicting that the barred gravitational potential produces a family of closed $x_2$ orbits perpendicular to the bar (e.g. Binney et al. 1991; Athanassoula 1992).

The 'elliptical orbit' model proposed by Molinari et al. (2011) was questioned by Kruijssen et al. (2015) and Henshaw et al. (2016). Kruijssen et al. (2015) identified a significant discontinuity between the dust ridge and the 20 and 50 km s$^{-1}$ clouds in the ($l$, $v$) space, suggesting that they cannot be part of the same coherent gas stream. Henshaw et al. (2016) confirmed this finding, showing that SgrB2 and the dust ridge clouds are not physically connected to Arm II (see Fig. 2). This is also the case in our interpretation, where SgrB2 and the dust ridge clouds are connected to Arm I. Moreover, Kruijssen et al. (2015) argued that the Molinari et al. model is unable to explain the presence of a third stream of gas identified in the dust ridge region (see Section 2). This led Kruijssen et al. (2015) to develop a new model, the 'open stream' model, where all the coherent features of gas identified in the observations lie along a single open ballistic orbit, rather than along a closed orbit. The model was obtained by integrating orbits in an empirically constrained Milky-Way potential (Launhardt, Zylka & Mezger 2002) and making the fit to the observed gas distribution and kinematics. In agreement with the observational constraints discussed in Section 5.1 (detection of dust ridge, 20 and 50 km s$^{-1}$ clouds in absorption at 70 μm and proper motion of Sgr B2), the 'open stream' model locates all the prominent molecular clouds in front of the Galactic Centre, even

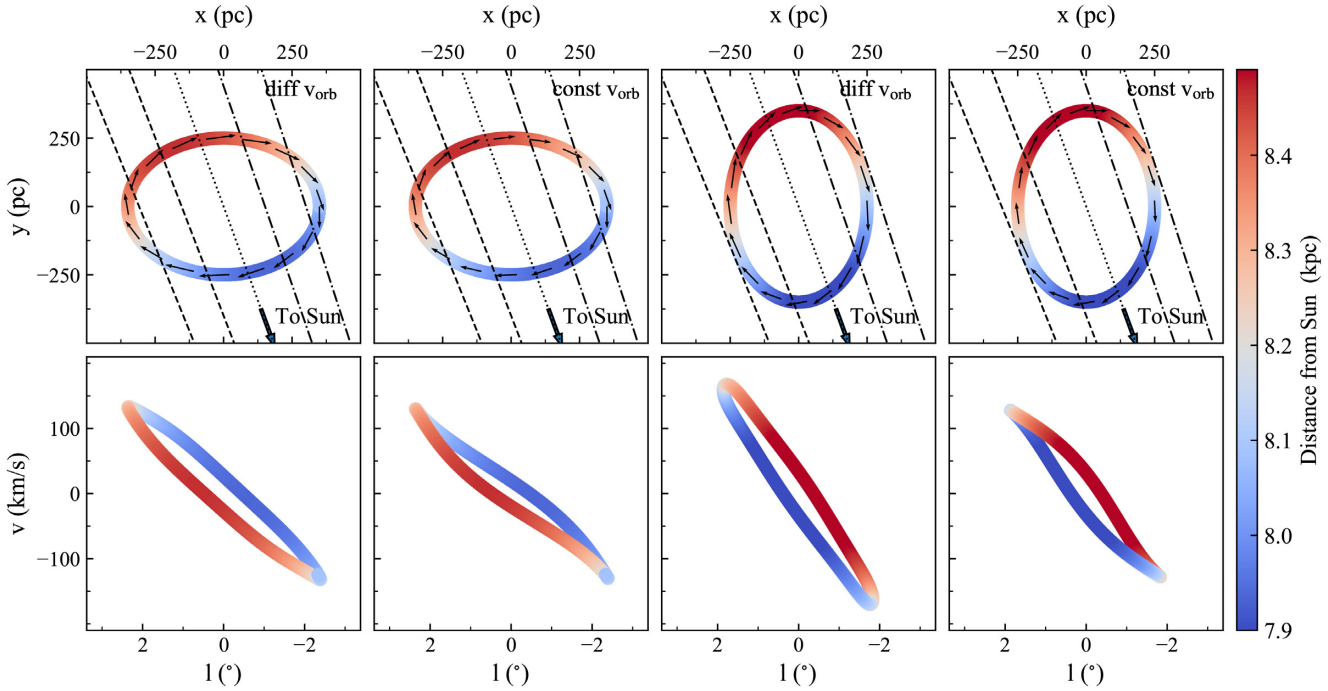


**Figure 9.** Models of possible ring configurations in the ($x$, $y$) (*top panels*) and ($l$, $v$) (*bottom panels*) space. In all the models, the bar major axis is always aligned with the axis $x = 0$ and the angle between the bar major axis and the Sun-Galactic Centre line is 20°. In the *first column* from the left, the ring minor axis is aligned with the bar major axis and the orbital velocity, $v_{orb}$, varies across the orbit. This configuration corresponds to the one produced in our simulation. In the *second column*, the ring minor axis is aligned with the bar major axis and the orbital velocity is constant. In the *third column*, the ring major axis is aligned with the bar major axis and the orbital velocity is variable. In the *forth column*, the ring major axis is aligned with the bar major axis and the orbital velocity is constant. The orbital velocity is shown in the top panels with vectors, whose length is proportional to the velocity magnitude. The different colours indicate the distance of each point from the Sun.

though on different segments of the orbit. Although this model appears to be the most successful proposed so far in reproducing the kinematics of dense gas (Henshaw et al. 2016), it does not attempt to capture the origin of the CMZ and its connection with the gas dynamics on larger scales. In our simulation, the Galactic bar induces gas to flow towards the Galactic Centre and that settles into a ring. We generally identify only two streams of gas in the position–longitude plot, corresponding to the two sides of the ring. However, it may happen that gas clouds depart from their $x_2$ orbit due to dissipative processes, producing structures not parallel to the two main streams and making the overall geometry more asymmetric.

A third model proposed to explain the gas distribution within the CMZ is the 'spiral arms' model (Sofue 1995; Sawada et al. 2004). This model assumes that the CMZ is dominated by two spiral arms, where the arm near the Sun corresponds to Arm I, while the arm farther from the Sun corresponds to Arm II. Ridley et al. (2017) re-proposed this model based on the analysis of their Milky-Way-like simulation. However, unlike Sofue (1995) and Sawada et al. (2004), they identified Arm I as the far spiral arm and Arm II as the near spiral arm. While Ridley et al. (2017) adopted the same gravitational potential as we use in our work, there are none the less several differences between the two simulations that might explain the different gas configuration in the CMZ. In Ridley et al. (2017), self-gravity and stellar feedback are not included and, more important, gas is assumed to be isothermal with an effective sound speed of 10 km s$^{-1}$. Sormani et al. (2018b) showed that the gas thermal pressure plays an important role in regulating the gas distribution within the CMZ.

We finally discuss our results in relation to the hypothesis that Sgr B2 and the dust ridge clouds represent a time-sequence of star-forming clouds (Longmore et al. 2013b). Observational studies of the dust ridge have indeed shown signs of increasing star formation activity with increasing the Galactic longitude (Lis et al. 2001). Based on the 'open streams' predictions that the dust ridge clouds are moving towards higher longitudes, Longmore et al. (2013b) proposed that star formation might be triggered by tidal compression during the passage of gas near the minimum of the Galactic potential. This would explain why Sgr B2, located at high longitudes, exhibits high level of star formation, while the Brick, which has just experienced its passage near the Sgr A*, shows no sign of star formation. In our simulation, we do not see evidence of gas compression in proximity of the Galactic Centre. Gas is mainly compressed in the regions where the dust lanes collide with the ring, i.e. close to major axis of the orbit. We have seen that, when the CMZ is in a quiescent period of star formation, many observed gas clouds are transient structures that are weakly bound or completely unbound, and may therefore slowly evaporate as they orbit. Therefore, according to our simulation, a time-sequence of star-forming clouds is more likely to form as a consequence of gas evaporation as the clouds move away from the dust lanes, rather than due to their passage near the Galactic Centre. However, we do warn that the strength of the tidal perturbations that clouds experience is a function of the orbits they take, and thus of the global potential. It is conceivable that tidal shocking might be more important for clouds in a ring that is closer to Sgr A* than that in our simulation. For example, recent simulations of individual molecular clouds orbiting in the Milky-Way potential empirically constrained by Launhardt

et al. (2002) have shown that at $R \sim 100$ pc, tidal perturbations can be effective in triggering the cloud gravitational collapse (Dale, Kruijssen & Longmore 2019).

Future observations will be valuable to distinguish among all the proposed models. We have seen that the H I emission is uniform across the ring and able to trace its entire structure. The ongoing GASKAP survey (Dickey et al. 2013) will provide high-resolution and high-sensitivity H I observations of the Galactic Centre, which might be useful to understand the large-scale gas distribution and dynamics in the CMZ. On the other side, ALMA observations of a variety of molecular transitions will give unprecedented details of individual molecular cloud properties.

### 5.3 Predictions for extragalactic nuclear regions

In Paper I, we suggested that the extreme environmental conditions typical of nuclear regions of barred spiral galaxies cause the star formation activity to go through burst/quench cycles, rather than reaching a steady-state equilibrium (see also Section 3.2 and Fig. 3). In the highly dense nuclear regions, the dynamical times of star formation are almost one order of magnitude smaller than the time required for stellar feedback to be effective. This might lead to a sudden gravitational collapse of the gas and a burst of star formation, which is suppressed only when stellar feedback significantly raises the local level of turbulence. This scenario is supported by observational studies showing that the nuclear regions of star-forming galaxies exhibit a much wider range of depletion times (ratio of the gas surface density to the star formation surface density) than the outer discs (variations over $\sim$1 dex, Leroy et al. 2013; Utomo et al. 2018).

In our model, variations in the depletion time are the result of cyclic variations in the SFR per unit gas mass, which is associated with a morphological transition in the gas distribution. This represents an observationally testable prediction. When the CMZ is near the minimum of a star formation cycle (SFR $\sim 0.1-0.2$ $M_\odot$ yr$^{-1}$), most of the gas lies in a ring-like structure, with the regions at higher density generally located near the intersection with the dust lanes. By contrast, when the CMZ is near the maximum of a star formation cycle (SFR $\sim 1-2$ $M_\odot$ yr$^{-1}$), the gas distribution is much less uniform, with a considerable part of the gas lying in star-forming molecular clouds, and a smaller part of it distributed in fragments of the pre-existing ring destroyed by supernova feedback. This reflects in a less coherent kinematical structure compared to the case with low star formation, which is detectable both through atomic and molecular gas emission.

The CMZ of our Galaxy only provides a single snapshot of the star formation cycle, and thus cannot provide a direct test of this prediction. However, detailed high-resolution observations of extragalactic CMZs can probe a diverse range of nuclear environments and star-forming states. Examining Figs 5 and 7, the morphological difference is clearly visible in a variety of molecular tracers. Thus, high-resolution maps of nuclear regions represent the best method available to test this prediction. Recently, Callanan et al. (submitted) have obtained ALMA observations in the innermost 500 pc of the barred galaxy M83 at a resolution scale of $\sim$10 pc. The nuclear regions of M83 presents gas properties (e.g. gas content, velocity dispersion, metallicity) similar to those of the Milky Way's CMZ (see also Israel & Baas 2001; Gazak et al. 2014). However, while our CMZ is currently producing stars at a rate lower than what expected from density-dependent star formation laws (SFR $\sim 0.1$ $M_\odot$ yr$^{-1}$), the centre of M83 is actively star-forming (SFR $\sim 2.5$ $M_\odot$ yr$^{-1}$, Muraoka et al. 2007). The factor of 25 difference in SFR might be explained by the fact that the CMZs of the Milky Way and M83 are undergoing different phases of their star formation cycles. In this scenario, the CMZ of the Milky Way would be currently near a minimum of a burst/quench cycle, while the CMZ of M83 would be near a maximum. Thus, the gas morphology in the centre of M83, and its level of clumping compared to that seen in the Milky Way, represents a useful test of our model. However, given the difficulties of comparing our face-on view of M83 to our edge-on view of the Milky Way, a much cleaner test would be to compare M83 to the morphology of another external galaxy with similar bulk properties, but with a present-day nuclear SFR more similar to that of the Milky Way than to M83.

## 6 CONCLUSIONS

The CMZ is a unique environment in our Galaxy characterized by extreme gas properties. Despite the gas densities orders of magnitude larger than those measured in the disc, the SFR is modest. Moreover, rather than being distributed relatively smoothly with radius as is the case elsewhere in the disc, gas in the CMZ is concentrated in a dense ring or stream structure at a limited range of galactocentric radii. In Paper I, we investigated the gas cycle and star formation history of the CMZ through a detailed hydrodynamical simulation of the inner 4.5 kpc of a Milky-Way-like galaxy. One of the main finding of Paper I is that star formation activity in the CMZ goes through oscillatory burst/quench cycles, with characteristic variability-time of $\sim$50 Myr mainly driven by stellar feedback instabilities.

In this work, we rerun part of the simulation analysed in Paper I at higher resolution. The goal is to perform a detailed study of the gas distribution and kinematics in the CMZ region. We run the high-resolution simulation for 50 Myr, during which the SFR increases by more than one order of magnitude. We then carry out a detailed chemical and observational post-process of the simulated CMZ in order to produce synthetic data cubes and maps of H I, CO ($J = 1 - 0$), $NH_3$ (1,1), and HCN ($J = 1 - 0$) emission. The major findings of our work are as follows:

(i) When the CMZ is near a minimum of its star formation activity, most of the gas lies in a dense elliptical ring. This translates into two elongated and nearly parallel streams of gas in the longitude–velocity map. The stream at higher velocities corresponds to the near side of the ring, while the stream at lower velocities corresponds to the rear side of the ring. Gas moves from positive longitudes and velocities to negative longitudes and velocities in the near ring side, and from negative longitudes and velocities to positive longitudes and velocities in the far ring side. While the H I distribution is nearly uniform across the ring, the molecular gas emission is asymmetric and predominantly clumpy. Generally, most of the emission comes from the high longitude and velocity (in absolute value) regions where gas orbiting within the ring collides with dust lane material.

(ii) Within the ring, shocks due to colliding flows and clouds readily produce dense regions ($n_H \gg 10^3$ cm$^{-3}$) that can be observed in tracers such as HCN and $NH_3$. However, the newly formed high-density regions do not necessarily evolve as gravitationally bound structures. Densities larger than $10^4$ cm$^{-3}$ are required for the gravitational collapse to start. Gas clouds that are not sufficiently dense slowly evaporates during their trajectory within the ring. The presence of large quantities of dense but unbound gas explains the low SFR per unit mass in the present-day CMZ. It also suggests that at least some of the clouds that are

not currently star-forming may never become so, and may instead evaporate due to hydrodynamic stripping.

(iii) The gas distribution and kinematics appear much less uniform and coherent when the CMZ is actively star-forming. Supernova feedback locally increases the level of turbulence, thus fragmenting the dense ring. Most of the gas lies in star-forming dense clouds rotating nearly in the same position of the pre-existing ring. The two elongated streams of gas in the longitude–velocity plot are replaced by ridges of gas with little extension in longitude and velocity in the H I map and bright clouds in the molecular emission maps. In extragalactic observations of CMZs similar to that of the Milky Way, but near the maximum of their star formation cycle, this difference in morphology should be detectable in high-resolution molecular line maps.

We identify some analogies between the observed features of the Milky Way's CMZ and the gas distribution predicted by our model when the CMZ is near the minimum of the SFR. In agreement with our findings, the molecular gas distribution of the present-day CMZ is highly asymmetric and dominated by two extended parallel streams in the longitude–velocity space. However, our model would locate Sgr B2 and the dust ridge clouds beyond the Galactic Centre, in contrast with some observational evidence suggesting that they should lie in front of the Galactic Centre. We conclude stressing that high-resolution observations over a variety of neutral and molecular gas transitions both in the Milky Way and extragalactic CMZs are still required to test the validity of our model against other possible interpretations.

## ACKNOWLEDGEMENTS

The authors thank the referee, Diederik Kruijssen, for his comments that have improved the clarity of this work. They also thank Adam Ginsburg and Steven Longmore for useful suggestions and Jonathan Henshaw for providing the fit to the $NH_3$ data made with SCOUSE. Simulations were performed on the Raijin supercomputer at the National Computational Infrastructure (NCI), which is supported by the Australian Government, through grant jh2. LA and MRK acknowledge support from the Australian Research Council's *Discovery Projects* and *Future Fellowships* funding schemes, awards DP190101258 and FT180100375. EDT acknowledges the support of the Australian Research Council (ARC) through grant DP160100723.

## REFERENCES

Ao Y. et al., 2013, A&A, 550, A135
Armillotta L., Krumholz M. R., Di Teodoro E. M., McClure-Griffiths N. M., 2019, MNRAS, 490, 4401
Athanassoula E., 1992, MNRAS, 259, 345
Bally J., Stark A. A., Wilson R. W., Henkel C., 1988, ApJ, 324, 223
Barnes A. T., Longmore S. N., Battersby C., Bally J., Kruijssen J. M. D., Henshaw J. D., Walker D. L., 2017, MNRAS, 469, 2263
Battersby C., Bally J., Svoboda B., 2017, ApJ, 835, 263
Binney J., Tremaine S., 2008, Galactic Dynamics. 2nd edn., Princeton Univ. Press, Princeton
Binney J., Gerhard O. E., Stark A. A., Bally J., Uchida K. I., 1991, MNRAS, 252, 210
Bitran M., Alvarez H., Bronfman L., May J., Thaddeus P., 1997, A&AS, 125, 99
Bland-Hawthorn J., Gerhard O., 2016, ARA&A, 54, 529
Bressan A., Marigo P., Girardi L., Salasnich B., Dal Cero C., Rubele S., Nanni A., 2012, MNRAS, 427, 127
Chabrier G., 2005, in Corbelli E., Palla F., Zinnecker H., eds, Astrophysics and Space Science Library, Vol. 327, The Initial Mass Function 50 Years Later. Springer-Verlag, Berlin, p. 41
Churazov E., Khabibullin I., Sunyaev R., Ponti G., 2017, MNRAS, 465, 45
Clark P. C., Glover S. C. O., Ragan S. E., Shetty R., Klessen R. S., 2013, ApJ, 768, L34
Clavel M., Terrier R., Goldwurm A., Morris M. R., Ponti G., Soldi S., Trap G., 2013, A&A, 558, A32
Coil A. L., Ho P. T. P., 2000, ApJ, 533, 245
da Silva R. L., Fumagalli M., Krumholz M., 2012, ApJ, 745, 145
Dale J. E., Kruijssen J. M. D., Longmore S. N., 2019, MNRAS, 486, 3307
Dame T. M., Hartmann D., Thaddeus P., 2001, ApJ, 547, 792
De Pree C. G. et al., 2014, ApJ, 781, L36
Dickey J. M., Lockman F. J., 1990, ARA&A, 28, 215
Dickey J. M. et al., 2013, Publ. Astron. Soc. Aust., 30, e003
Draine B. T., 1978, ApJS, 36, 595
Federrath C. et al., 2016, ApJ, 832, 143
Ferland G. J. et al., 2013, Rev. Mex. Astron. Astrofis., 49, 137
Ferrière K., Gillard W., Jean P., 2007, A&A, 467, 611
Gazak J. Z. et al., 2014, ApJ, 787, 142
Gentry E. S., Krumholz M. R., Madau P., Lupi A., 2019, MNRAS, 483, 3647
Ginsburg A. et al., 2016, A&A, 586, A50
Gong M., Ostriker E. C., Wolfire M. G., 2017, ApJ, 843, 38
Hasegawa T., Sato F., Whiteoak J. B., Miyawaki R., 1994, ApJ, 429, L77
Henshaw J. D. et al., 2016, MNRAS, 457, 2675
Hopkins P. F., 2015, MNRAS, 450, 53
Hopkins P. F. et al., 2018a, MNRAS, 477, 1578
Hopkins P. F. et al., 2018b, MNRAS, 480, 800
Immer K., Menten K. M., Schuller F., Lis D. C., 2012, A&A, 548, A120
Indriolo N., McCall B. J., 2012, ApJ, 745, 91
Israel F. P., Baas F., 2001, A&A, 371, 433
Jones P. A. et al., 2012, MNRAS, 419, 2961
Kim C.-G., Ostriker E. C., 2015, ApJ, 802, 99
Kim W.-T., Stone J. M., 2012, ApJ, 751, 124
Krieger N. et al., 2017, ApJ, 850, 77
Kruijssen J. M. D., Longmore S. N., 2013, MNRAS, 435, 2598
Kruijssen J. M. D., Longmore S. N., Elmegreen B. G., Murray N., Bally J., Testi L., Kennicutt R. C., 2014, MNRAS, 440, 3370
Kruijssen J. M. D., Dale J. E., Longmore S. N., 2015, MNRAS, 447, 1059
Kruijssen J. M. D. et al., 2019, MNRAS, 484, 5734
Krumholz M. R., 2014, MNRAS, 437, 1662
Krumholz M. R., Gnedin N. Y., 2011, ApJ, 729, 36
Krumholz M. R., Kruijssen J. M. D., 2015, MNRAS, 453, 739
Krumholz M. R., Tan J. C., 2007, ApJ, 654, 304
Krumholz M. R., Fumagalli M., da Silva R. L., Rendahl T., Parra J., 2015, MNRAS, 452, 1447
Krumholz M. R., Kruijssen J. M. D., Crocker R. M., 2017, MNRAS, 466, 1213
Launhardt R., Zylka R., Mezger P. G., 2002, A&A, 384, 112
Le Petit F., Roueff E., Herbst E., 2004, A&A, 417, 993
Leitherer C. et al., 1999, ApJS, 123, 3
Leroy A. K. et al., 2013, AJ, 146, 19
Li Z., Gerhard O., Shen J., Portail M., Wegg C., 2016, ApJ, 824, 13
Lis D. C., Serabyn E., Zylka R., Li Y., 2001, ApJ, 550, 761
Longmore S. N. et al., 2013a, MNRAS, 429, 987
Longmore S. N. et al., 2013b, MNRAS, 433, L15
Longmore S. N. et al., 2017, MNRAS, 470, 1462
McGrath E. J., Goss W. M., De Pree C. G., 2004, ApJS, 155, 577
McMillan P. J., 2017, MNRAS, 465, 76
Molinari S. et al., 2011, ApJ, 735, L33
Morris M., Serabyn E., 1996, ARA&A, 34, 645
Muraoka K. et al., 2007, PASJ, 59, 43
Offner S. S. R., Krumholz M. R., Klein R. I., McKee C. F., 2008, AJ, 136, 404
Oka T., Nagai M., Kamegai K., Tanaka K., Kuboi N., 2007, PASJ, 59, 15
Oka T., Geballe T. R., Goto M., Usuda T., Benjamin, McCall J., Indriolo N., 2019, ApJ, 883, 54

Onus A., Krumholz M. R., Federrath C., 2018, MNRAS, 479, 1702
Purcell C. R. et al., 2012, MNRAS, 426, 1972
Reid M. J., Menten K. M., Brunthaler A., Zheng X. W., Moscadelli L., Xu Y., 2009, ApJ, 693, 397
Ridley M. G. L., Sormani M. C., Treß R. G., Magorrian J., Klessen R. S., 2017, MNRAS, 469, 2251
Rodriguez-Fernandez N. J., Combes F., 2008, A&A, 489, 115
Rodríguez-Fernández N. J., Martín-Pintado J., Fuente A., Wilson T. L., 2004, A&A, 427, 217
Safranek-Shrader C., Krumholz M. R., Kim C.-G., Ostriker E. C., Klein R. I., Li S., McKee C. F., Stone J. M., 2017, MNRAS, 465, 885
Sato F., Hasegawa T., Whiteoak J. B., Miyawaki R., 2000, ApJ, 535, 857
Sawada T., Hasegawa T., Handa T., Cohen R. J., 2004, MNRAS, 349, 1167
Seo W.-Y., Kim W.-T., Kwak S., Hsieh P.-Y., Han C., Hopkins P. F., 2019, ApJ, 872, 5
Shetty R., Beaumont C. N., Burton M. G., Kelly B. C., Klessen R. S., 2012, MNRAS, 425, 720
Shin J., Kim S. S., Baba J., Saitoh T. R., Hwang J.-S., Chun K., Hozumi S., 2017, ApJ, 841, 74
Smith B. D. et al., 2017, MNRAS, 466, 2217
Sofue Y., 1995, PASJ, 47, 527
Sormani M. C., Binney J., Magorrian J., 2015, MNRAS, 449, 2421
Sormani M. C., Treß R. G., Ridley M., Glover S. C. O., Klessen R. S., Binney J., Magorrian J., Smith R., 2018a, MNRAS, 475, 2383
Sormani M. C., Sobacchi E., Fragkoudi F., Ridley M., Treß R. G., Glover S. C. O., Klessen R. S., 2018b, MNRAS, 481, 2
Sormani M. C. et al., 2019, MNRAS, 488, 4663
Springel V., 2005, MNRAS, 364, 1105
Sukhbold T., Ertl T., Woosley S. E., Brown J. M., Janka H.-T., 2016, ApJ, 821, 38
Utomo D. et al., 2018, ApJ, 861, L18
van der Tak F. F. S., van Dishoeck E. F., 2000, A&A, 358, L79
Walsh A. J. et al., 2011, MNRAS, 416, 1764
Wegg C., Gerhard O., Portail M., 2015, MNRAS, 450, 4050
Wolfire M. G., McKee C. F., Hollenbach D., Tielens A. G. G. M., 2003, ApJ, 587, 278
Yusef-Zadeh F. et al., 2009, ApJ, 702, 178

## APPENDIX A: RADIATION FIELD MODELS

To establish which of the four radiation models (see Section 3.3) is more representative of the present-day CMZ, we perform a few comparisons between the gas properties predicted by the four models and those measured in the CMZ. First of all, we derive the molecular gas mass, $M_{\rm mol} = 2 m_{\rm H} n_{\rm H} X_{\rm H_2} / \mu_H$, where $\mu_{\rm He} = 1.36$ is the helium correction based on cosmological abundances, and the $H_2$ abundance, $X_{\rm H_2}$, is an output of DESPOTIC. We find that the molecular mass is roughly constant with time, it varies by less than a factor 1.5 for all the models. Among them, the *Solar* model predicts $M_{\rm mol} \sim 6 \times 10^7\,{\rm M}_\odot$, while the three CMZ models predict $M_{\rm mol} \sim 1.5{-}2.5 \times 10^7\,{\rm M}_\odot$. We point out that the *Solar* model and the CMZ model predictions are consistent with the upper and lower limit of the observationally inferred masses ($M_{\rm CMZ} \sim 2{-}7 \times 10^7\,{\rm M}_\odot$), respectively. However, the latter are measured for the entire inner 500 pc region of our Galaxy. The molecular mass in the central 2° of the Milky Way – which is the region that we compare with the dense ring formed in the simulation – is $\sim$1.8 $\times$ $10^7\,{\rm M}_\odot$ (Longmore et al. 2013a), in agreement with the predictions of the CMZ radiation models. However, we note that the molecular mass in the CMZ is often inferred using CO ($J = 1 - 0$) emission measurements (e.g. Ferrière et al. 2007). Translating from $L_{\rm CO}$ to $M_{\rm mol}$ relies on the choice of the CO-to-$H_2$ conversion factor, $\alpha_{\rm CO} \equiv M_{\rm mol}/L_{\rm CO}$. Since our models independently predict the total CO luminosity and the $H_2$ mass, we can evaluate $\alpha_{\rm CO}$ in our models, and compare to inferences of this same quantity in the observed CMZ obtained by comparing dust and CO maps. We find that the $\alpha_{\rm CO}$ oscillates around $1.5\,{\rm M}_\odot$ (K km s$^{-1}$ pc$^2$)$^{-1}$ for all the CMZ models, in agreement with the value inferred in the present-day CMZ (Kruijssen et al. 2014).

As a second test, in Fig. A1, we evaluate the gas temperature distribution as calculated with DESPOTIC as a function of $n_{\rm H}$. The *Solar* model (first panel) predicts gas temperatures well below the actual gas temperature produced in the simulation, especially at $n_{\rm H} \lesssim 10^2$ cm$^{-3}$. This is because the photoelectric heating rate (Section 3.1) used in the simulation is chosen to mimic an ISRF significantly stronger than that found in the Solar neighbourhood, and thus the transition from warm neutral medium (WNM, $T \sim 10^4$ K) to cold neutral medium (CNM, $T \lesssim 100$ K) occurs at higher gas densities in the simulation than in the post-processed table for the *Solar* case. The three CMZ radiation field models all produce similar WNM/CNM transitions, but differ in the temperatures they predict in dense and shielded gas at $n_{\rm H} \sim 10^4$–$10^5$ cm$^{-3}$. In particular, the temperatures predicted by the *weak* model, $T_{\rm g} \sim$ 15–60 K (second panel), are in agreement with those characteristic of the cold molecular component ($T \sim$ 25–50 K, Krieger et al. 2017), while the temperatures predicted by the *strong* model, $T_{\rm g} \sim$ 40–180 K (fourth panel), are in agreement with the observed temperatures of the warm molecular component ($T \sim$ 60–150 K, Krieger et al. 2017). As expected, the *intermediate* model (third panel) produces intermediate temperatures between the two previous models, $T_{\rm g} \sim$ 25–100 K. This result clearly suggests that the radiation field in

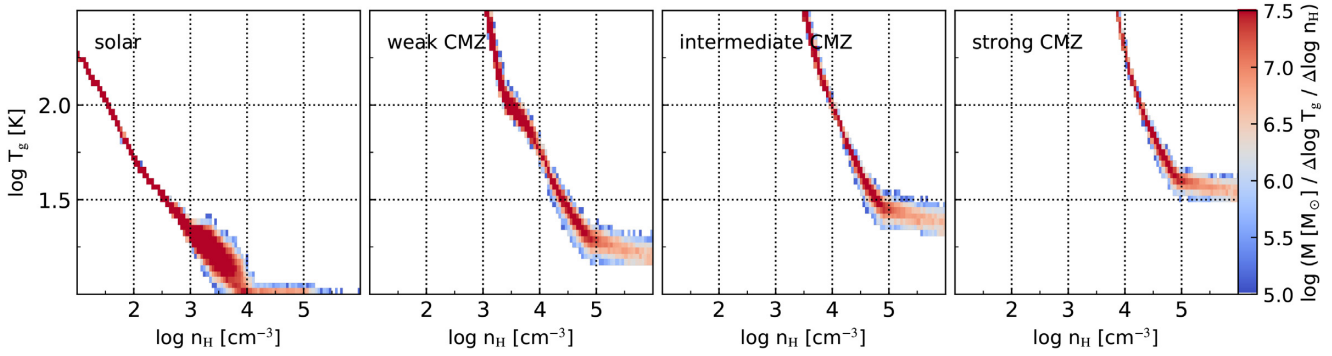


**Figure A1.** Temperature-density phase diagram of the CMZ as calculated with DESPOTIC for four different radiation field models, *Solar* ($\chi = 1\,G_0$ and $\zeta = 10^{-16}$ s$^{-1}$, *first panel*), *weak* CMZ ($\chi = 10^2\,G_0$ and $\zeta = 10^{-15}$ s$^{-1}$, *second panel*), *intermediate* CMZ ($\chi = 10^{2.5}\,G_0$ and $\zeta = 10^{-14.5}$ s$^{-1}$, *third panel*), and *strong* CMZ ($\chi = 10^3\,G_0$ and $\zeta = 10^{-14}$ s$^{-1}$, *fourth panel*). The diagram is computed as a two-dimensional histogram showing the mass of gas particles within each logarithmic bin, normalized by the bin area. The temperature–density distributions have been calculated at $t = 505$ Myr.

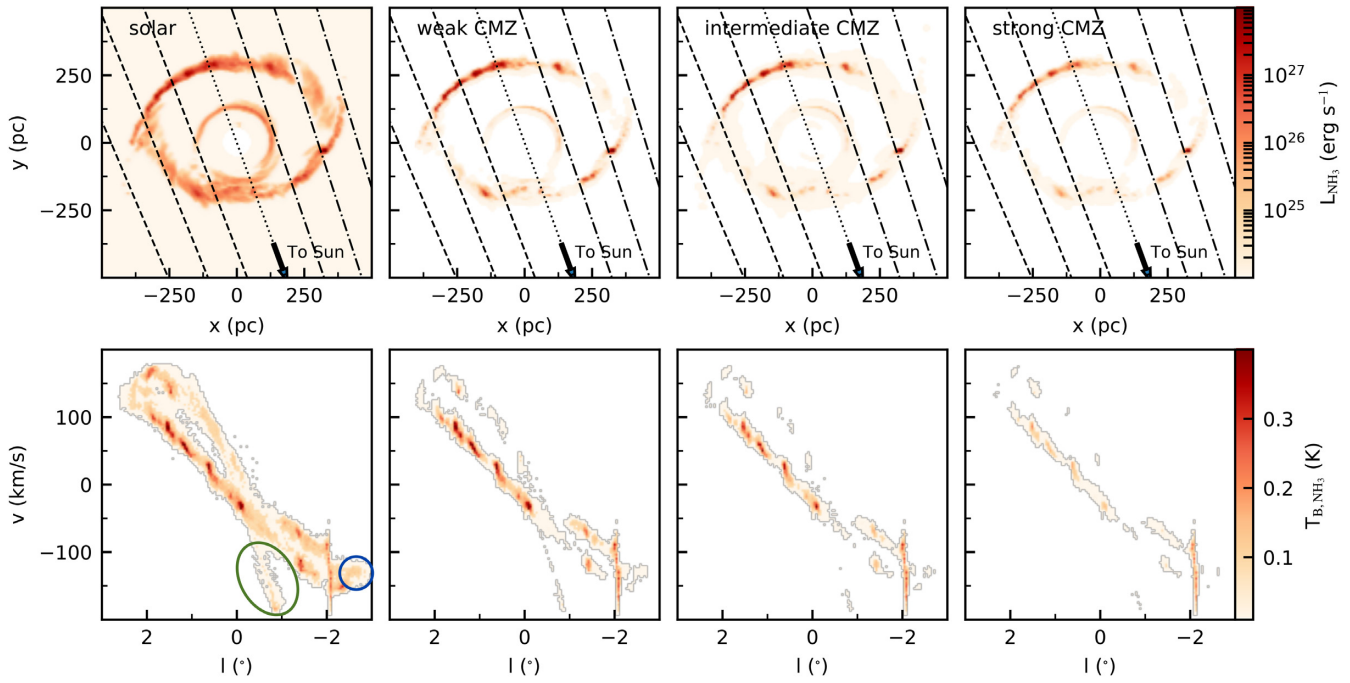


**Figure A2.** Cartesian distribution of the $NH_3$ (1,1) luminosity (*upper panels*) and $NH_3$ (1,1) brightness temperature distribution in the longitude–velocity diagram (*lower panels*) obtained assuming four different radiation field models, *Solar* (*first column*), *weak* CMZ (*second column*), *intermediate* CMZ (*third column*), and *strong* CMZ (*fourth column*). The coloured contours denote relevant structures discussed in the main text. The snapshots have been taken at $t =$ 505 Myr.

the present-day CMZ is not constant, but instead varies based in the local star formation conditions. Given the best match with the observations in terms of temperature, we adopt the *intermediate* CMZ radiation model as the fiducial model throughout this work.

To understand the sensitivity of our results to this choice, in Fig. A2 we compare the distribution of $NH_3$ (1,1) emission predicted by the four models at $t = 505$ Myr. The $NH_3$ (1,1) luminosity becomes weaker and weaker with increasing ISRF and cosmic ray fluxes as a consequence of the different gas temperature and molecular gas mass predicted by the different models. The *Solar* radiation model predicts high luminosities ($L_{NH_3} > 10^{26}$ erg s$^{-1}$) across the entire ring. This allows us to clearly detect all the prominent features in the longitude–velocity map that are discussed in the main text: the two elongated parallel streams corresponding to the two sides of the ring, the ridge of molecular clouds in the far side of the ring, and also the low-density inner ring at $R \sim$ 100 pc (green contour) that we have seen to be mainly composed of atomic gas under the assumption of *intermediate* CMZ radiation field (see Section 4.1). On the other hand, under the assumption of *strong* CMZ radiation field, the $NH_3$ (1,1) brightness temperatures are very low ($T_{B,NH3} \lesssim 0.2$ K) even in regions with relatively high density ($n_H \lesssim 10^4$ cm$^{-3}$). The blue contour in the *Solar* ($l$, $v$) map highlights the dust lane side immediately connected to the ring. The brightness temperature associated with this region becomes a factor of 2 lower for the *weak* CMZ radiation field compared to the *Solar* case, and nearly zero assuming *intermediate* or *strong* radiation. As noted above, it is very likely that the radiation field is not constant throughout the CMZ region, but instead varies depending on local star formation activity. Therefore, we cannot exclude the possibility that regions such as the dust lanes, where little star formation occurs, might experience a less intense radiation field and produce higher brightness temperatures than those predicted in our fiducial, *intermediate* case.

This paper has been typeset from a TEX/LATEX file prepared by the author.